Review

A Review on van der Waals Boron Nitride Quantum Dots

Amit Acharya [1,2], Sambhawana Sharma [1,2], Xiuling Liu [1,3], Dongyan Zhang [1,2,*] and Yoke Khin Yap [1,2]

1. Department of Physics, Michigan Technological University, Houghton, MI 49931, USA; amitacha@mtu.edu (A.A.); ssharma5@mtu.edu (S.S.); xiulingl@mtu.edu (X.L.); ykyap@mtu.edu (Y.K.Y.)
2. Elizabeth and Richard Henes Center for Quantum Phenomena, Michigan Technological University, Houghton, MI 49931, USA
3. StabiLux Biosciences, Inc., Ann Arbor, MI 48103, USA
* Correspondence: dozhang@mtu.edu; Tel.: +1-906-487-2086

Abstract: Boron nitride quantum dots (BNQDs) have gained increasing attention for their versatile fluorescent, optoelectronic, chemical, and biochemical properties. During the past few years, significant progress has been demonstrated, started from theoretical modeling to actual application. Many interesting properties and applications have been reported, such as excitation-dependent emission (and, in some cases, non-excitation dependent), chemical functionalization, bioimaging, phototherapy, photocatalysis, chemical, and biological sensing. An overview of this early-stage research development of BNQDs is presented in this article. We have prepared un-bias assessments on various synthesis methods, property analysis, and applications of BNQDs here, and provided our perspective on the development of these emerging nanomaterials for years to come.

Keywords: quantum dots; boron nitride; van der Waals; fluorescent; sensing; photocatalysis

1. Introduction

Low dimensional boron nitride (BN) materials such as BN nanosheets and BN nanotubes (BNNTs) have gained substantial attention [1–9]. BN materials are isoelectric to carbon solids. For example, the three-dimensional (3D) cubic phase (c-BN), two-dimensional (2D) hexagonal phase (h-BN), and one-dimensional (1D) BN nanotubes (BNNTs) are structurally like diamonds, graphene, and carbon nanotubes (CNTs), respectively. Despite these structural similarities, BN materials offer different physical and chemical properties. For instance, all BN materials are electrically insulating with about 6eV bandgaps, while most carbon nanomaterials are metallic, except semiconducting single-walled CNTs [10]. Like other 2D materials such as graphene [11], and transitional metal dichalcogenides (TMDC), 2D BN nanosheets have gained significant research attention [12–14]. Boron nitride nanoribbons, the 1D version of BN nanosheets, are also attractive for their spintronics, magnetic, and electronic properties [15–18]. More recently, zero-dimensional (0D) BN quantum dots (BNQDs) or BN dots (BNDs) have emerged as the new BN nanomaterials, with extremely high surface/volume ratios. Many optical and electronic properties of BNQDs are yet to be clarified and therefore are expected to stimulate a lot more theoretical and experimental investigation.

BNQDs are a 0D version of h-BN nanosheets. Due to their small dimension, the ratio of dangling bonds at the edges of BNQDs to the saturated sp^2 h-BN bonds on the bulk of the 0D structure is high. It is expected that these edges will alter the physical and chemical properties of the h-BN nanosheets. Their high chemical stability and the non-toxic nature of BN materials are expected to allow for many biomedical applications in BNQDs. The theoretical study of electronic structures and spin polarization in BNQDs was first conducted in 2011 [19] based on first-principle calculations and an extended Hubbard model. Later in 2013, similar studies [20,21] on the structural stability, electronic, optical, and magnetic properties of BNQDs were performed. Experimentally, BNQDs synthesis [22,23] was reported thereafter. As shown in Figure 1, the number of peer-reviewed publications has

significantly increased during the past two years. This publication statistic has considered papers consisting of the keyword "boron nitride quantum dots", and did not include papers with other 0D boron nitride nanoparticles. Two recent review articles briefly discussed 0D BN materials along with other BN nanoparticles [24,25]. In this article, we will focus on reviewing the recent development of BNQDs, from the synthesis, characterization, and various applications.
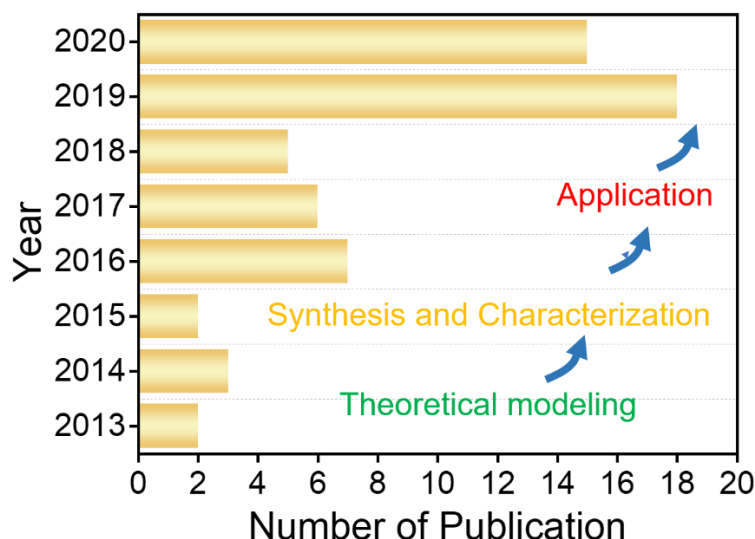

Figure 1. The number of papers published with title or topic containing boron nitride quantum dots (BNQDs) based on Web of Science ^{TM} analysis with the keyword "boron nitride quantum dots".

2. Crystal Structures

BN is the lightest III-IV compound and is isoelectric to carbon structures by sharing the same total number of electrons between the neighboring atoms [26]. As shown in Figure 2a, BN has different polymorphs, including hexagonal BN (h-BN), cubic BN (c-BN), rhombohedral BN (r-BN), and wurtzite BN (w-BN) [27–31]. The h-BN and r-BN have sp^2 hybridized B-N bonds while the c-BN and w-BN are sp^3 hybridized. The h-BN phase is the most stable phase under standard conditions, consists of strong boron–nitrogen covalent intralayer bonds making hexagonal planar geometry and weak van der Waals interaction between layers in the bulk state as shown in Figure 2b. There is also electrostatic interaction due to the electronegativity difference between the boron and nitrogen atoms between adjacent layers [32] in the interlayer stacking. Unlike electron distribution in the graphene C-C bond, the electrons in the B-N bond move towards the electronegative N atoms vacating the boron atoms and provide a partial ionic character through polarization of the B-N bond. The basal planes in h-BN are stacked in an alternating AA'AA' . . . sequence which is different when compared with graphite in which hexagonal nanosheets are stacked in the ABAB sequence. The w-BN has a diamond-like tetrahedral structure with similar AA'AA' staking to that of h-BN. The r-BN has a three-fold stacking sequence ABCABC . . . as shown in Figure 2a. Similarly, the stacking sequence for c-BN is like that of r-BN but has a tetrahedral structure. In this review, we will discuss only the stable h-BN materials.
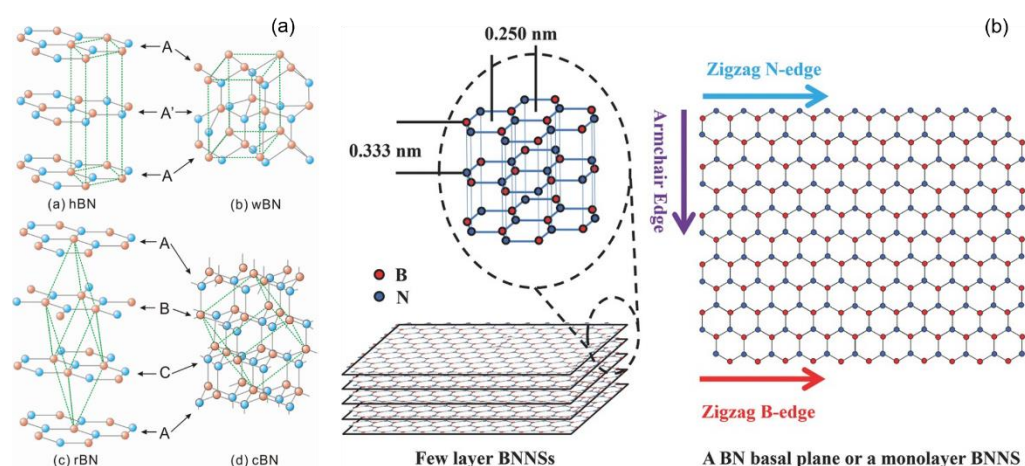
Figure 2. (**a**) Crystal structures of h-BN, w-BN, r-BN, and c-BN. Boron atoms are shown in red, while nitrogen atoms are shown in blue [28]. Reproduced with permission. 2007 IOP Publishing Ltd. (**b**) Structural basis for two-dimensional h-BN nanostructures, where B-N bonds have the length of 0.145 nm, the distance between two adjacent borazine rings is 0.250 nm, and the interlayer distance is 0.333 nm. The edge of the monolayer BN nanosheet can be either zigzag or armchair [13]. Reproduced with permission. Copyright 2017 WILEY-VCH Verlag GmbH & Co. kGaA (Weinheim, Germany).

3. Synthesis of BNQDs

Experimental research on BNQDs is still at an early stage. BNQDs can be synthesized via top-down or bottom-up approaches. For the top-down process, bulk h-BN powder is exfoliated into thinner nanosheets and subsequently into QDs by combining various processes. For the bottom-up approach, B and N precursors are used to grow the BNQDs. Both approaches have their advantages and shortcomings. BNQDs obtained by exfoliation have good crystallinity but are poly-dispersed in size. The weak van der Waals interaction between h-BN nanosheets makes the exfoliation possible; however, the strong in-plane covalent bonds are preventing the formation of 0D structures. Breaking the h-BN sheet into 0D is time-consuming, and the yield is low. In contrast, the bottom-up approach allows for better control in the shape and size of BNQDs, but the crystallinity is relatively inferior to those produced by the top-down approach.

3.1. Top-Down Approaches

The top-down method is the most used method for the exfoliation of layered structure materials due to its relative simplicity and effectiveness. Researchers have used the micromechanical cleavage method, also called the scotch tape method, to obtain the BN nanosheets by repeatedly peeling the adhesive tape from the bulk h-BN sample up to the monolayer [33,34]. This method could produce BN nanosheets with a lateral size of 100 micrometers. Other methods such as liquid exfoliation, defect engineering, and chemical exfoliation were used to obtain the BN nanosheets, which were further assisted with sonication and heating to obtain the BNQDs. These methods are discussed in detail here.

3.1.1. Sonication-Assisted Liquid Exfoliation Method

This process involves the use of liquids to disperse bulk h-BN powders, followed by high-power sonication and refluxing. The polarity of liquid is the important parameter in liquid exfoliation and is usually directly proportional to the surface energy [35] to overcome the weak van der Waals force between the h-BN layers. Liquid with higher polarity would strongly interact with h-BN layers, facilitating easier exfoliation to BN nanosheets and then to BNQDs. Various liquids used in the production of BNQDs are discussed here.

Water: Stengl et al. [22] were the first research group to make BNQDs using sonication-assisted liquid exfoliation and heating. They first prepared h-BN particles by annealing boric acid and urea under a nitrogen atmosphere. These h-BN particles were then exfoliated

in water to obtain BN nanosheets using a high-intensity cavitation field in a pressurized batch reactor. The products were further refluxed at 198 °C in ethylene glycol at atmospheric pressure for 48 h. The resulting dispersion was filtered off using a membrane filter to obtain a clear and transparent solution that contains BNQDs. The heat treatment broke the BN nanosheets in a boiling solution to produce few-layered BNQDs whose surface was passivated by the ethylene glycol chains. The as-prepared BNQDs showed excitation-dependent emission, i.e., the fluorescent/luminescent wavelength is tunable by using different excitation wavelengths. Figure 3 shows the excitation-dependent photoluminescence (PL) spectra of h-BN QDs, excited at a wavelength from 290 to 400 nm [36]. Transmission electron microscopy (TEM) revealed non-uniform crystallinity comprising r-BN and some amorphous BN. This work was inspired by previous works in the making of graphene QDs and carbon QDs [37,38]. Similar experiments to obtain BNQDs from chemically exfoliated h-BN (using H_2SO_4 and $KMnO_4$) did not yield any QDs.
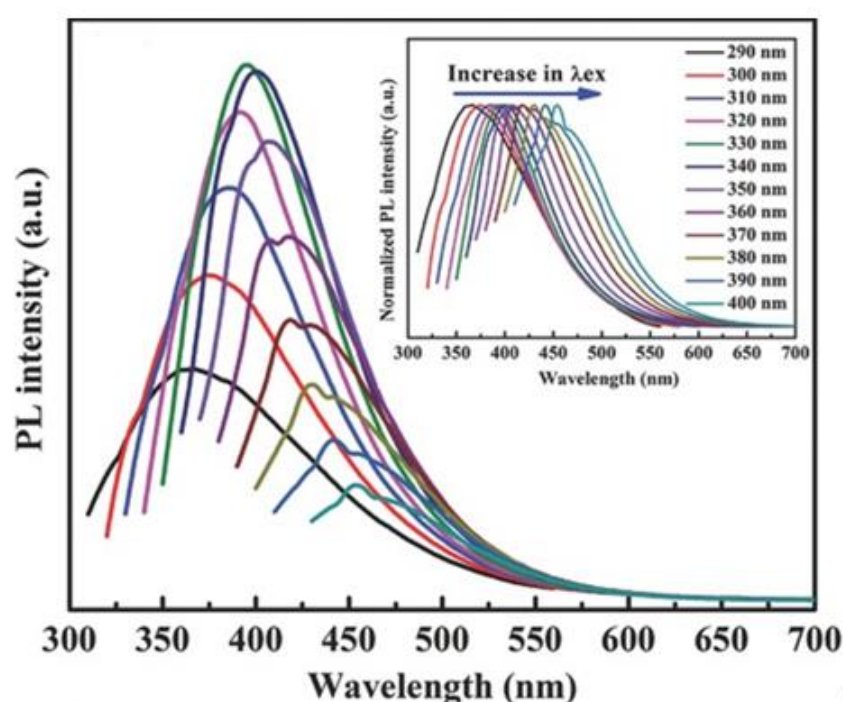

Figure 3. Photoluminescence (PL) of h-BN quantum dots showing excitation-dependent emission. The inset plot shows the corresponding normalized PL spectra [36]. Reproduced with permission. Copyright 2015 WILEY-VCH Verlag GmbH & Co. kGaA (Weinheim, Germany).

Organic solvents: Li et al. [36] reported on the fabrication of BNQDs with controllable size using sonication in dimethylformamide (DMF) and the subsequent solvothermal process as illustrated in Figure 4. They reported on the size control of BNQDs with an average size of 2.62 nm. A fluorescent quantum yield (QY) of up to 19.5% was obtained by adjusting the solvothermal synthesis parameters, such as filling factor, synthesis temperature, and process duration. Similar methods were later adopted by various research groups using different organic solvents, such as DMF, dimethyl sulfoxide (DMSO), ethanol, isopropyl alcohol (IPA), and *N*-methyl-2-pyrrolidone (NMP) [39–41]. Liu et al. reported the synthesis of BNQDs with tunable blue/green PL using three solvents (ethanol, DMF, and NMP) in their liquid exfoliation-solvothermal treatment. The authors observed blue fluorescence from samples prepared in ethanol and DMF, but green fluorescence from samples prepared in NMP under the same UV irradiation. These results suggest that the sizes, QY, and optical properties of these BNQDs were dependent on the polarity of different organic solvents. The PL for BNQDs prepared in ethanol was reported to show excitation-independent emission. In contrast, BNQDs prepared in DMF and NMP were demonstrating excitation-

dependent emission. The quantum yields (QYs) and average lateral sizes of the BNQDs are reported as 12.6% and 4.1 ± 0.2 nm, 16.4% and 2.8 ± 0.3 nm, as well as 21.3% and 2.0 ± 0.2 nm for samples prepared in ethanol, DMF, and NMP, respectively [40].
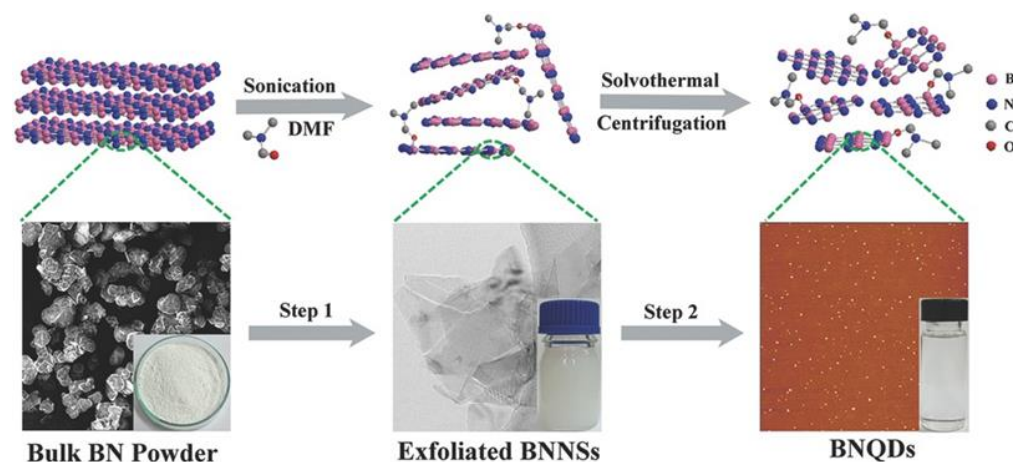

Figure 4. Schematic illustration of the BNQD synthesis procedure, including the sonication-assisted liquid exfoliation of h-BN bulk powder to synthesize BN nanosheets and solvothermal treatment to fabricate BNQDs [36]. Reproduced with permission. Copyright 2017 WILEY-VCH Verlag GmbH & Co. kGaA (Weinheim, Germany).

Fan et al. reported the use of a microwave irradiation technique to synthesize BNQDs. These BNQDs are 1.98 to 7.05 nm in size with a high QY of 23.44% and excellent electromagnetic wave absorption performance. The author reported synthesizing BN nanoplates (BNNPs) from bulk h-BN powder using tip ultrasonication in DMF as illustrated in Figure 4. The BNNPs' dispersion was irradiated with microwaves in a solvothermal process at 150 °C for 10 min. The products were then centrifuged and finally filtered with microporous membrane filters to obtain BNQDs. The size and dispersity of the as-prepared BNQDs were reported to be tuned with reaction temperature and duration time of microwave irradiation [42].

Acid: Kumar et al. reported a facile, scalable, and single-step method to make BNQDs using high-intensity sonication. This approach resulted in the exfoliation and etching of BN nanosheets in Bronsted acid (H_3PO_4 in this case). The majority of BNQDs were formed by the etching at the edge site of BN nanosheets. The average size of synthesized particles was 3–6 nm and thickness 3–12 atomic BN layers [43].

Base: Xue et al. [44] fabricated fluorescent monolayer BNQDs with an average lateral size of around 3.3 nm, an average thickness of 1.05 nm, and a QY of 1.8%. The authors use a hydrothermal method by breaking the bulk h-BN powders into a basic solution. The bulk h-BN powder was mixed and grounded with sodium hydroxide and potassium hydroxide (KOH), and then heated in an autoclave. The products were then centrifuged to obtain BN nanosheets. These exfoliated BN nanosheets were again hydrothermally treated with water and KOH to create defects in the BN nanosheets which were further tip sonicated and filtered to obtain BNQDs. A similar synthesis approach for BNQDs was reported by Dehghani et al. [45] using liquid exfoliation of hBN in KOH and ethanol, followed by hydrothermal treatments. The as-synthesized BNQDs emit blue fluorescence. After surface passivation with polyethylene glycol (PEG_{200}), these BNQDs produce green emission under the same UV irradiation. These BNQDs have an average size of 1.8 ± 0.3 nm, an average thickness of 2 ± 0.5 nm, and a QY of 32% for blue fluorescence, and 38% for green fluorescence. These BNQDs also demonstrate excellent dispersion in water. The synthesis of highly water-soluble BN nanosheets and BNQDs was simultaneously reported by Liu et al. [46] using solvothermal treatment of bulk h-BN in ethanol with the presence of sodium hydroxide (NaOH). Their method relies on the insertion of Na^+ and OH^- ions into the BN layers at high temperature and pressure, thus exfoliating it layer by layer, and

finally breaking into BN nanosheets and BNQDs. They reported the yield of BN nanosheets and BNQDs to be as high as 18.1% and 2.9%, respectively.

3.1.2. Defect Engineering Method

In this method, defects are created on an atomic scale using different physical sources such as microwaves, lasers, and ion beams. These defects work as active nucleation sites for covalent bonding between two hetero nanostructures. Jung et al. reported a defect engineering method to synthesize the blue luminescent BNQDs and edge-hydroxylated BNQDs (EH-BNQDs) from bulk h-BN powders using physical energy sources including an impinging process of heated iron nanoparticles, microwave irradiation, and sonication as illustrated in Figure 5. This process helped disintegrate bulk BN not only at the edges but also on the surfaces. The as-prepared BNQDs had poly-dispersed sizes ranging from 10 to 50 nm with an average thickness of 3.2 nm. A relatively low QY of $1.19 \pm 0.34\%$ was obtained from such BNQDs. The QY for EH-BNQDs was 0.7%. The decrease in QY for the latter was due to the reduction of defect sites by hydroxylate groups [47].
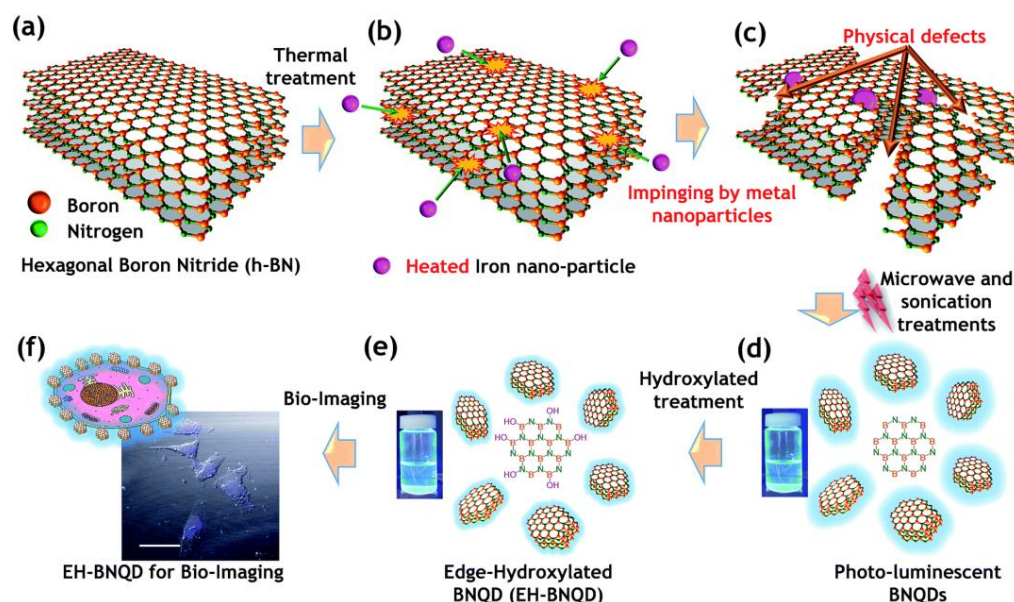
Figure 5. Defect engineering route to boron nitride quantum dots (BNQDs) and edge-hydroxylated BNQDs for bioimaging. (**a**) Hexagonal boron nitride, (**b**) impinging process of heated iron nanoparticles, (**c**) cracks and physical defects of h-BN, (**d**) BN QD after microwave radiation and sonication treatments, (**e**) edge-hydroxylated BN QD (EH-BN QD), and (**f**) EH-BN QD for bioimaging. Reproduced from [47] with permission from The Royal Society of Chemistry.

3.1.3. Intercalation Method

Lin et al. [23] adopted the same approach to prepare BNQDs as they did previously for graphene QDs [48] by exfoliating and disintegrating h-BN flakes. Their approach included potassium (K) intercalation between noncovalently bonded h-BN nanosheets, de-intercalation by short exposure of K-hBN to air, and disintegration of BN edges by reacting K-hBN and ethanol-water under ultrasonic treatment. Monolayered BNQDs with an average lateral size of 10 nm were obtained. These QDs have a QY of 2.5% after the introduction of oxidized defect centers (e.g., BO_2^-, carbene zigzag edge, C replaced N vacancy point) that caused a blue-green luminescence. Also, with the decrease in the thickness and size of QDs, strong quantum confinement was seen, which increased the optical band gap to 6.51 eV in comparison to 6 eV of the bulk h-BN powders.

Peng et al. [49] reported another synthesis method of BNQDs by the intercalation of hydrazine hydrate (N_2H_4) into the BN interlayer space of h-BN powders using the solvothermal technique. This was followed by ultrasonic treatment in water/ethanol

mixture solution to obtain BN nanosheets. After evaporating ethanol and adjusting the pH to 8 with KOH, the obtained BN nanosheets were hydrothermally treated to obtain BNQDs after filtration using a microporous membrane. These BNQDs have lateral sizes and thicknesses in the range of 1–2.6 and 0.86–1.18 nm, respectively. A fluorescence QY of 4.16% was obtained. Furthermore, the as-prepared BNQDs were reported to exhibit excitation-independent fluorescence emission. This result suggests that fluorescence was due to the same surface states rather than the particle size-dependent quantum confinement effect. Besides, as-prepared BNQDs were reported to show high thermostability, prominent anti-photobleaching capability, good salt tolerance stability, and pH-independence ability [49].

3.1.4. Other Methods

Thangasamy et al. [50] reported a supercritical fluid (SCF) approach for rapid (within 40 min) and facile synthesis of blue luminescent BNQDs. These QDs exhibit an average lateral size of 5 nm and a fluorescence QY of 2.8% from bulk BN via in situ exfoliation followed by disintegration. SCF has the combination of vapor and liquid properties such as low interfacial tension, excellent wetting of surfaces, and high diffusion coefficients required for efficient exfoliation/functionalization [51–54] and was created by increasing the temperature and pressure of the solvent (DMF) above its critical levels, where distinct liquid and gas phases do not exist. Their results also showed the existence of oxygen doping and more important adsorption of DMF molecules on the BNQD surface, which was not reported previously.

Angizi et al. [55] reported the mechanochemical exfoliation approach of the synthesis of hydroxylated (-OH) functionalized BNQDs in ethanol. These BNQDs exhibit an average thickness of 2 nm, an average lateral dimension of 4 nm, and a QY of 6.2%. This approach included high-energy ball milling (up to 16 h) in wet conditions (ethanol). Such a process grinds and exfoliates bulk h-BN powders to BN nanosheets because of shear and normal stress. Such a process was followed by solvothermal treatment in ethanol for 18 h at 250 °C to enhance -OH functionalized BNQDs. The reported spectroscopic analysis showed that the occurrence of interaction between oxygen groups of the solvent and boron sites of h-BN has led to efficient exfoliation of h-BN and -OH functionalized BNQDs, as aided by mechanical forces. The authors correlate the blue PL fluorescence to the oxygen-and carbon-based emission centers. This excitation-independent PL suggests uniform surface states on BNQDs. The authors continued to explore the possibility of other methods for the surface/edge functionalization of BNQDs [56]. They reported the use of various solvents—ethanol, ethylenediamine, and DMF for the hydroxyl, amine, and methyl functionalization of BNQDs, respectively—and studied their effects on the QD bandgap. They applied the same mechanochemical exfoliation approach to synthesize BNQDs in these solvents. The polarity of these solvents ranged from 4.3 (ethanol) to 6.4 (DMF). It was demonstrated that and the use of solvents with higher polarities yielded better exfoliation efficiencies. The authors reported the bandgap modification of BNQDs using chemical molecule interaction with dangling bonds. The splitting of the main transition bandgap of bulk BN from 5.9 eV to two absorption edges for hydroxyl (2.3–3.6 eV), methyl (3.2–4.2 eV), and amine (3.1–4 eV) was evident from UV-Vis absorption and PL plots. They correlate these absorptions to delocalizing of the P_x and P_z orbitals due to edge/surface functional groups (hydroxyl, methyl, and amine) as explained earlier. The chemical motifs provided by the solvents at high temperature and pressure interacted with the boron sites on BNQDs, resulting in the decrease in optical bandgap due to different surface functionalization.

Cai et al. [57] reported the turbulence-induced disintegration method by the use of a food blender to prepare BNQDs from bulk BN crystals in isopropanol (IPA) and de-ionized water. The high-shear turbulence flow generated by the blender would break down the interlayer van der Waals forces between h-BN layers, and disintegrate them into QDs with an average lateral size of 2.13 ± 0.25 nm and thicknesses of 0.6 to 4 nm while using IPA. These average particle sizes are about double when water was used in the blending process. They introduced the formation mechanism of BNQDs based on fluid dynamics. In the case

of IPA, the calculated Reynolds number was 1.37×10^6 and the mean turbulent shear rate was 2.34×10^4 s^{-1}, both above the threshold value of 10^4 for both parameters required for the exfoliation of nanoflakes to QDs. The particle yield was reported to be 4.02%.

Radhakrishnan et al. [58] reported the synthesis of fluorinated BNQDs (FBNQDs) by the hydrothermal fluorination of BN nanosheets using DMF and Nafion. Nafion acted as the source for highly reactive fluorine-free radicals which reacted with BN nanosheets to break it down to form FBNQDs. They reported the fluorination using different solvents, DMF and formamide, where the latter gave higher vapor pressure, which was considered an important parameter for fluorination. This heterostructure of FBNQDs was reported to decrease the optical band gap of h-BN and have broad-spectrum light absorption with luminescence in the blue-green region and a high QY of 19.5%.

Duong et al. [59] reported the synthesis of BNQDs using the cryogenic-mediated exfoliation of h-BN powders, as assisted with ultra-sonication and filtration. As reported, the bulk powders were soaked in liquid nitrogen for an hour and thermally shocked by introducing a mixture of IPA and water (1:1 ratio). This process created the peeling of h-BN flakes and formed cracks and defects in all dimensions. Further, ultrasonication induced full liquid-phase exfoliation. After centrifuging and filtration, the obtained BNQDs had narrow size distribution with sizes as small as 3 nm. These BNQDs contained fluorescent point defects that acted as photostable single-photon emitters which can be used as fluorescent markers in bioimaging applications and are suitable for far-field super-resolution fluorescence nanoscopy.

In summary, the top-down methods are based on reducing the bulk h-BN powders to nanometer sizes using different approaches. Poor material yield is problematic for mass production, but the crystallinity is excellent. The dangling bonds at the edges of BNQDs and surface defects will allow for the functionalization of various molecules, which makes BNQDs prospective for fluorescent and optoelectronic applications.

3.2. Bottom-Up Approaches

The top-down approach used for the synthesis of BNQDs requires lengthy processing of bulk h-BN powders and involves some complicated post-process treatment such as centrifugation and filtration. To tackle some of these problems, the bottom-up method could be utilized where QDs can be synthesized by using atomic, ionic, or molecular starting materials. Various groups have utilized such bottom-up approaches to synthesize BN nanostructures which included hydrothermal [60–62] and chemical vapor deposition (CVD) methods [63]. Some of these bottom-up approaches for the synthesis of BNQDs will be discussed in this section.

3.2.1. Hydrothermal Methods

Liu et al. [64] were the first group to adopt the bottom-up approach to synthesize hydroxyl-and amino-functionalized BNQDs. The BNQDs exhibit a lattice constant of 0.22 nm, an average thickness of 0.91 nm, a particle size of 2.56 to 3.20 nm within reaction times of 9 to 15 h, and a high QY of 18.3%. The authors hydrothermally treated the mixture of boric acid and ammonia solution in one pot at 200 °C for 12 h. The mechanism for the hydrothermal reaction and fluorescence quenching was also modeled theoretically using density functional theory (DFT). The UV absorption at a wavelength of 229 nm was reported which matched the DFT. Two sharp excitation peaks at 230 and 295 nm were detected, which are different from those previously reported [23,39] and were attributed to the difference in the chemical environment. As shown in Figure 6, excitation-independent fluorescence was reported suggesting that the PL properties are due to specific surface states rather than the particle sizes of the QDs. A similar method for BNQDs synthesis was reported later with slight or no modification [65–69].
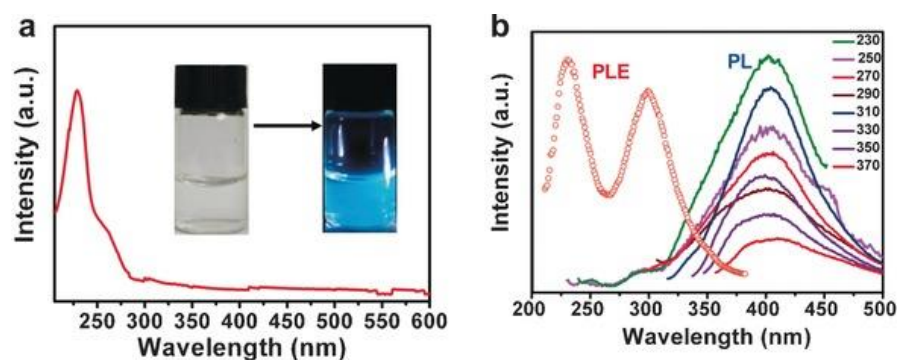
Figure 6. (**a**) UV-Vis absorption; inset: photographs of the BNQDs dispersed in aqueous solution under visible (left) and λ = 365 nm UV (right) lights. (**b**) Photoluminescence excitation (PLE) spectrum of the prepared BNQDs and excitation-independent PL emission behavior of BNQDs excited at different wavelengths from λ = 230–370 nm. Reproduced from [64] with permission from 2016 Wiley-VCH Verlag GmbH & Co. KGaA (Weinheim, Germany).
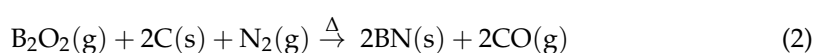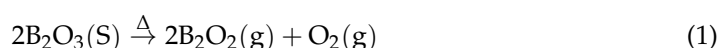
Researchers are finding alternative sources of nitrogen for the bottom-up synthesis of BNQDs because ammonia solutions are volatile, pollution, irritative, and harmful to human tissues. Huo et al. [70] reported the use of melamine as the nitrogen source and boric acid as the boron source for the synthesis of BNQDs by the economical hydrothermal method. The as-grown BNQDs have an average lateral size of 3 nm, and an average thickness of 0.7 nm. A similar aqueous synthesis method of BNQDs was reported by others [71–73]. Later, Liu et al. [74] used the microwave method to synthesize BNQDs with a QY 10.31% by dissolving boric acid and melamine in ultra-pure water and placing them in a microwave oven set at a frequency of 1000 Hz for 70 min at 120 °C. The authors also reported for the synthesis of sulfur S-regulated BNQDs using the same microwave method and same precursors (boric acid and melamine) [75]. They reported the use of thiourea and L-cysteine as the sulfur precursors, which yielded S-regulated BNQDs with different optoelectronic, electrochemiluminescence (ECL), and electro-optical properties. The use of different sulfur precursors introduced different functional groups on the surfaces of BNQDs, which would result in electron transitions, as verified by zeta potentials, UV-Vis absorption, and FTIR spectroscopy measurements. Interestingly, the QYs for S-regulated BNQDs prepared with thiourea and L-cysteine were 8.9% and 2.0%, respectively, both lower than for pristine BNQDs (10.31%) due to additional nonradiative pathways introduced by the sulfur dopants. Besides, the authors reported that the PL and ECL behaviors (emission peak) strongly depend on the surface states and functional group of the S-regulated BNQDs. Recently, Yasno et al. [76] reported the short-time microwave method in the synthesis of BN nanoparticles with a disc-like morphology using boric acid and melamine as raw materials using a 2.4 GHz microwave field for 90 min.

Besides melamine, researchers have attempted to use urea dissolved in ammonia solution as the nitrogen source. For example, Jerome et al. have synthesized BNQDs by the hydrothermal method by using such a nitrogen source and boric acid dissolved in ethanol/water as the boron source [77]. The same boron and nitrogen source were used by other research groups [78] for BNQDs synthesis. Another hydrothermal method was reported by Yao et al. [79] for the fabrication of BNQDs with a high QY of 32.3%. These BNQDs have an average size of 4 nm and were made by using boric acid and ammonium hydroxide as starting materials. Besides, Kong et al. [80] have reported on the hydrothermal synthesis of BNQDs using amino acids (tryptophan) as a nitrogen source and boric acid as a boron source. As compared to other nitrogen precursors, amino acids are high in nitrogen content, good in biocompatibility, and low in price. The as-prepared BNQDs exhibit spherical shapes with an average diameter of 3.05 ± 0.57 nm, and a QY of 8.45%. These BNQDs initiated a strong absorption peak at 280 nm, and always emit the same PL peaks when excited with different excitation wavelengths ranging from 280 to 400 nm (excitation independent). The authors have explored the use of other amino acids for the

synthesis of BNQDs. All these BNQDs exhibit strong blue fluorescence but their UV-Vis absorption peaks and PL emission spectra are varying. These results suggest the role of different surface states were formed on BNQDs, which are corresponding to varying optical and spectroscopic properties.

3.2.2. Carbothermal Reduction Reaction

Zhao et al. [81] have reported a different bottom-up approach towards the mass production of BNQDs with a QY as high as 18.2%. This was based on a biomass-directed strategy from steam-exploded rice straw lignin (SERSL). This work was inspired by a similar approach used for the growth of BN nanosheets based on carbothermal reduction [82]. The BNQD formation mechanism can be represented by the following reaction equations:

$$2B_2O_3(S) \xrightarrow{\Delta} 2B_2O_2(g) + O_2(g) \tag{1}$$

$$B_2O_2(g) + 2C(s) + N_2(g) \xrightarrow{\Delta} 2BN(s) + 2CO(g) \tag{2}$$

As shown in Figure 7, the B_2O_3 solid powders were converted into the B_2O_2 and oxygen vapors at temperatures above 1000 °C. The carbon atom at the defect sites of SERSL will then be oxidized by oxygen. The B_2O_2 vapors will then react with the activated carbon atoms near the dangling bonds and gradually replace the graphite's honeycomb lattice with B and N to form BN nanosheets. To prevent the formation of BCN/BN complexes during the reaction, the ratio of B_2O_3 to SERSL was optimized in the range 5:1 to 7:1. The optimum growth time was over 4 h, at temperatures above 1200 °C. Unlike another bottom-up approach of BNQDs synthesis, this method yielded BNQDs with excitation-dependent emission.
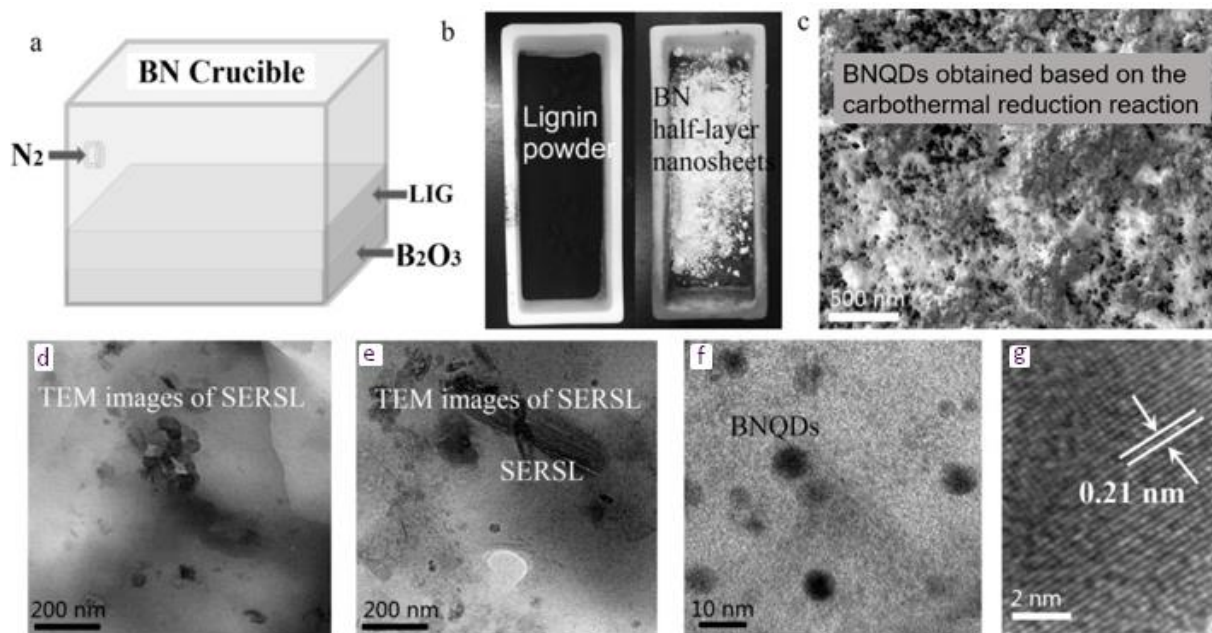

Figure 7. (**a**) Schematic for the synthesis of BN half-layer nanosheets from steam-exploded rice straw lignin (SERSL). SERSL covered the surface of B_2O_3 powder inside the crucible and was heated at 1300 °C in nitrogen atmosphere. (**b**) The optical images before (left) and after (right) reaction. The BN half-layer nanosheets were sonicated in dimethylformamide (DMF) to obtain BNQDs. (**c**) The SEM image of BNQDs. (**d**,**e**) The TEM images of SERSL. The low-resolution (**f**) and high-resolution (**g**) TEM images of BNQDs. Reproduced from [81] with permission from 2019 Wiley-VCH Verlag GmbH & Co. KGaA (Weinheim, Germany).

3.2.3. Other Methods

Ahmad et al. [83] reported the fabrication of large BN particles with a beads shape and an average lateral size of 50–200 nm. This was performed in a 25 min growth duration at 1200 °C using carbon-free precursors. The reported precursors comprised of nanosized B, magnesium oxide, and Maghemite (γ-Fe_2O_3) mixed in the ratio 2:1:1. The precursors were loaded in an alumina boat and heated in a horizontal tube furnace in ammonia gas as the nitrogen source for the formation of BN particles.

3.3. Combined Method

Li et al. [84] used the combined bottom-up and top-down approaches. Firstly, boron trioxide (B_2O_3) and urea ($CO(NH_2)_2$) were mixed in a molar ratio of 1:10 in methanol to form a transparent solution under stirring. The white crystalline precursor was obtained after 24 h, which was further grounded and heated at high temperatures under ammonia (NH_3) to produce ultrathin BN nanosheets. Secondly, the obtained BN nanosheets were treated ultrasonically and solvo-thermally in DMF to obtain BNQDs in a top-down manner. These BNQDs exhibit blue-green PL with a QY of 10%. The as-prepared BNQDs were reported to have oxygenous functional groups on the surface that had a strong influence on their PL characteristic.

4. Applications of BNQDs

4.1. Biological Application

Metal-free quantum dots such as carbon and BN quantum dots (CQDs, BNQDs) have multiple advantages over conventional semiconductor quantum dots. It is believed that CQDs and BNQDs exhibit higher photophysical, chemical, and photochemical stability. Besides, CQDs and BNQDs are non-toxic and more biocompatible [39,85]. It was reported that BNQDs are more biocompatible than carbon QDs as the latter would undesirably interact with biomolecules (DNA, proteins, or enzymes) that would compromise the intrinsic properties of these biomolecules [70]. Besides, BNQDs are more tolerant of different pH environments in the range of 2–12, with no significant effect on the fluorescence of BNQDs [40]. The cytotoxicity and biocompatibility of BNQDs were studied; excellent biocompatibility was shown [23,36,39,40,44,45,47,57,81].

4.1.1. Bioimaging

Organic dyes are popular for bioimaging applications for their relatively low cost and good biocompatibility. However, organic dyes are limited by photobleaching where their fluorescence brightness is degrading under the prolonged irradiation of excitation laser light. The use of nanoparticles such as BNQDs with strong fluorescence, photo-stable, nonblinking, and nonbleaching would be a good alternative for cellular imaging probes. Lin et al. have reported on the use of BNQDs for the imaging of MDCK-II (Madin-Darby canine kidney) cells by confocal microscopy in the FITC (fluorescein isothiocyanate) mode as shown in Figure 8. The BNQDs were internalized into cells but did not penetrate the cell nuclei [23]. A similar study was performed on different types of cells by others [39,40,44,46,57,81]. Jung et al. [47] studied the internalization of edge-hydroxylated BNQDs (EH-BNQDs) by MCF-7 breast cancer cells and PC-3 prostate cancer cells. Blue fluorescence in the perinuclear region was demonstrated. The locations of EH-BNQDs inside the cells were compared with the locations of intracellular endosomes that were labeled with Lysotracker (red dyes), which resulted in a purple color due to the overlapping of blue and red fluorescence under confocal microscope proving the successful endocytosis of QDs. A similar study was performed on HeLa cells [40].
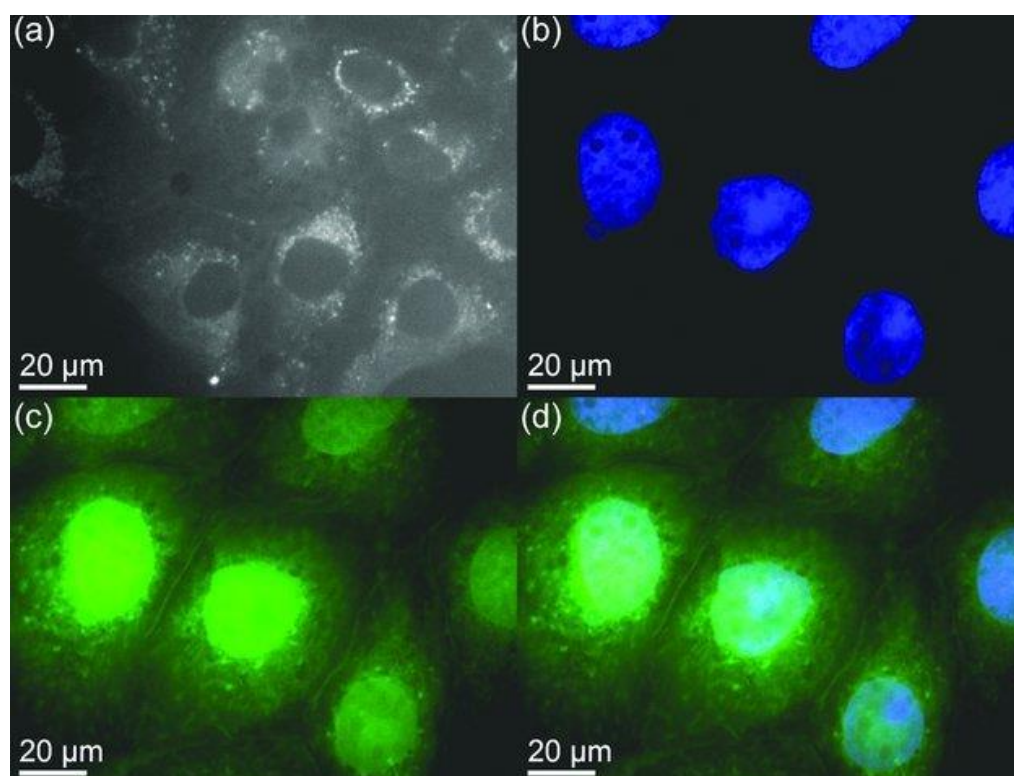
Figure 8. Confocal microscopy images of mammalian cells. (**a**) Agglomerated BNQDs surrounding each nucleus (cells are stained by BNQDs only). (**b**) Individual nucleus stained blue with DAPI (4′, 6-diamidino-2-phenylindole). (**c**) BNQDs with green luminescence surrounding the nuclei. (**d**) The overlay image of cells stained with DAPI and BNQDs. Reproduced from [23] with permission from 2013 Wiley-VCH Verlag GmbH & Co. KGaA (Weinheim, Germany).

　　　Thangasamy et al. [50] reported the imaging of bacterial cells (Gram-negative and Gram-positive) using BNQDs. Both types of cells were stained with 100 μg/mL of BNQDs. According to images from epi-fluorescence microscopy and confocal microscopy, the internalization of BNQDs occurred for Gram-negative cells but not for Gram-positive cells. It is to be noted that the Gram-negative cells possess an extra lipid layer outside the peptidoglycan layer, which Gram-positive cells lack. This interesting interaction of BNQDs with the outer lipid layer of Gram-negative cells can be used for Gram-negative cell identification and selective staining from environmentally mixed bacterial samples.

　　　BNQDs exhibit a long fluorescent lifetime (FLT) and a unique excitation-dependent emission property. Therefore, BNQDs can be a good candidate for multiplex fluorescence imaging when used in conjunction with organic dyes. The combined fluorescent signals can be resolved spectrally and temporally based on the emission wavelength and the FLT, respectively. For multiple probes having overlapping emission wavelengths but different fluorescent lifetimes, both spectral and temporal imaging can be combined. Dehghani et al. [45] reported the use of two-photon excitation features of BNQDs for multiplex cell imaging. The fluorescence lifetime imaging microscopy (FLIM) was used to accurately distinguish the emission signals of BNQDs with longer FLT in comparison to relatively shorter cell autofluorescence and those from organic dyes. They reported the use of two nuclear stains: DAPI (4′, 6-diamidino-2-phenylindole) with blue and Sytox with green fluorescence, both with shorter fluorescent decay lifetimes, to achieve the temporally and spectrally resolved fluorescent signals as shown in Figure 9. They co-stained the RL-14 cells with b-BNQDs/DAPI (b-BNQDs: blue-emitting BNQDs) and g-BNQD/Sytox green (g-BNQDs: green-emitting BNQDs) separately. The emission of BNQDs and dyes was not separated by spectral analysis of the image, but this issue was resolved by using the difference in fluorescence lifetimes of BNQDs and dyes using the FLIM technique.
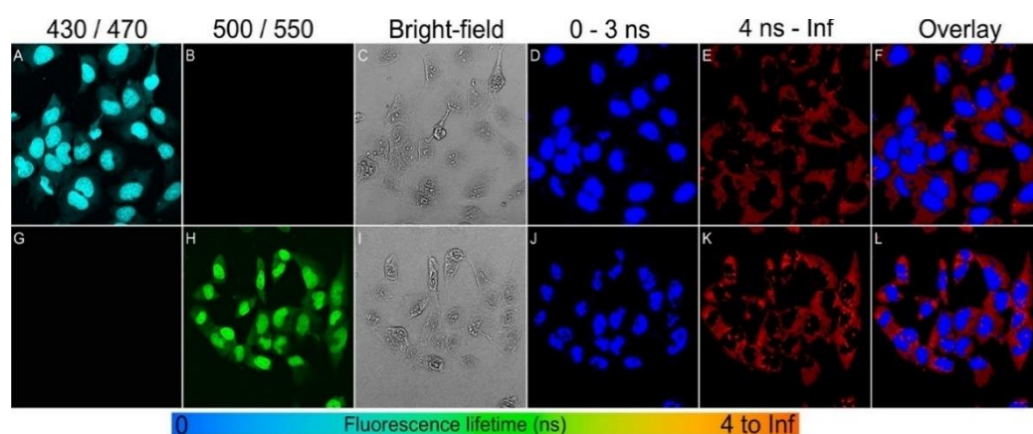
Figure 9. Spectral imaging (**A–C,G–I**) and fluorescence lifetime imaging (**D–F,J–L**) of RL-14 cells separately treated with b-BNQDs/DAPI and g-BNQDs/Sytox green. No emission was detected in panels B and G co-stained with QDs and stains. Fluorescence signals from b-BNQDs and g-BNQDs were resolved using spectrally matched detection ranges as seen in panels A and H. The fluorescence lifetimes were obtained by bi-exponential fitting and mapped to a false-color scale from 0 ns (blue) to >4 ns (red). The resulting false-color shows the difference between signals originating from BNQDs (panels D and J) and organic dyes (**E,K**). Reproduced from [45] with permission from Copyright © 2018 American Chemical Society.

4.1.2. Biosensing

Angizi et al. reported the use of BNQDs for the sensitive and selective detection of vitamin C (VC) [55]. This was performed by a modified screen-printed gold electrode (GSPE) with functionalized BNQDs. BNQDs are superior to carbon nanostructures in terms of the linear range of sensing and the detection limit. For example, a detection limit of 0.45 μM was recorded in Angizi et al.'s work while using the BNQDs/Au system, significantly lower than 3 μM for the cellulose acetate/graphite system. The high electrocatalytic activity for electro-oxidation of VC was reported and the oxidation occurred at the surface of the BN QD/Au electrode at a lower positive potential than the GSPE. Later, Jerome et al. [77] reported a rapid response sensor (1.8 sec) to detect vitamin C (ascorbic acid, AA) using BNQDs and polyluminol (Plu) coated glassy carbon electrode (GCE). As-prepared hybrid Plu/BNQDs coated GCE was reported to show improved electrocatalytic activity for AA oxidation at 0.2 V using the amperometry detection method. Further, they carried out the interference effects in the presence of uric acid, dopamine, and glucose which did not respond to the Plu/BNQDs/GCE sensors, indicating good selectivity of the sensor for AA. In another study, Kong et al. [80] reported a fluorescent "on-off-on" sensor to detect AA with Fe^{3+} as a medium. The fluorescence of BNQDs was quenched due to the inner filter effect between Fe^{3+} and BNQDs. Then, the fluorescence of BNQDs was restored with increasing AA due to the oxidation-reduction between Fe^{3+} and AA. This technique enabled the detection of AA in the concentration range 1–100 μM with a detection limit of 0.0833 μM under the optimized experimental conditions at pH 6. The sensing selectivity of BNQDs to Fe^{3+} ions was confirmed by comparing data obtained by using other metal ions. Other metal ions had a negligible effect on quenching BNQD fluorescence. The selectivity of BNQDs on AA sensing was also verified by replacing AA with other interfering substances, such as uric acid, dopamine, and glucose. These substances have shown little recovering effect on the fluorescence of BNQDs. All these data support the fact that BNQDs exhibit high selectivity for Fe^{3+} and AA.

Dehghani et al. [45] reported the use of g-BNQDs passivated with polyethylene glycol, for the biosensing of intracellular pH variations and their distribution inside cells. This was performed by confocal microscopy and FLIM techniques. It is to be noted that the increase in incubation time will cause the micro-environment of the cells to become more acidic due to the formation of more endosomes. The acidic environment would result in a shorter FLT.

The authors reported the translocation and accumulation of g-BNQDs at endosomes over 4 h, which resulted in the change of cell morphology. The quenching of photoluminescence of BNQDs in an acidic medium can be utilized for detecting changes in metabolic activity inside human cells. Owing to the Warburg effect [86], lactate production in cancer cells during glycolysis is high. Therefore, the extracellular pH of tumor cells is often acidic, leading to a high extracellular acidification rate (ECAR) compared to benign cells. Radhakrishnan et al. [58] reported the use of the glycolytic inhibitor, 3-bromopyruvate(3-BP), to suppress ECAR. This was demonstrated by monitoring the increase in fluorescence from FBNQDs, as a method to detect the glycolytic activity in cancer cells. In this case, the green fluorescence channel of flow cytometry was used to detect the enhanced fluorescent signal after introducing 3-BP to cancer cells. There was no considerable change in fluorescence in benign cells due to a less active glycolytic pathway. In another study, Yola et al. [41] reported a stable, repeatable, reusable, and selective imprinted biosensor based on BNQDs for cardiac Troponin-I (cTnI) detection in plasma samples. The cTnI is widely used for the diagnosis of acute myocardial infarction (AMI) diseases. Later, the same group [87] reported the preparation of a novel voltammetry sensor for the detection of various organophosphate pesticides in water samples based on BNQDs on graphene oxide.

Owing to the strong inner filter effect between 2,4,6-trinitrophenol (TNP) and BNQDs, the fluorescence intensity of BNQDs can be reduced upon quenching by TNP. By this mean, TNP can be selectively and sensitively detected in the concentration range of $0.25-200$ μM, with a detection limit of 0.14 μM when BNQDs are used as fluorescence probes [49]. Therefore, BNQDs can be used as the turn-off sensors for the rapid detection of TNP from natural water sources without tedious pretreatment processes. Similarly, Peng et al. [67] reported a "switch on" nanosensor for sensitive assay of glutathione (GSH). GSH can regulate the inner filter effect of MnO_2 nanosheets (NS) on BNQDs. Owing to the superior light absorption capability of redox-able MnO_2NS centered at 380 nm, the fluorescence of BNQDs (with a maximum emission wavelength 380 nm) can be selectively quenched. For an optimal inner filter effect to take place between the two substances, the maximum absorption of one should overlap the maximum emission of the other. However, the introduction of GSH will help to recover the fluorescence of BNQDs, dependent on the concentration of GSH, by weakening the inner filter effect as initiated by the decomposition of MnO_2 to Mn^{2+}. This MnO_2NS/BNQDs nanoprobe was reported to exhibit good selectivity on GSH detection in the range of 0.5–250 μM with a detection limit of 160 nm in human plasma samples. They reported the use of other interference substances such as histidine, glutamic acid, cysteine, vitamin C, sodium chloride, potassium chloride, etc., instead of GSH in the same concentration which did not show much change in fluorescence recovery, thus suggesting the need for the separation of interfering reductants from real samples. The sensing principle is shown in Figure 10.

In addition to the inner filter effect, fluorescence resonance energy transfer (FRET) on BNQDs also offers interesting application. For example, FRET between BNQDs and gold nanoparticles (AuNPs) has enabled the fabrication of rapid, label-free, and highly sensitive fluorescence-based biosensors [88]. Such sensors were used to detect acetylcholinesterase (AChE), a key enzyme in the biological nerve conduction system, whose activities have been connected to several diseases such as muscular paralysis, convulsions, and bronchial constriction. As reported, AChE can hydrolyze acetylthiocholine (ATCh) to generate thiocholine (TCh) whose thiol (-SH) group can reduce chloroauric acid ($HAuCl_4$) to AuNPs. The formation of TCh-BNQDs/AuNPs aggregates can quench the fluorescence of BNQDs via FRET. An inhibitor, paraoxon, was used to lower the activity of AChE and decreased the fluorescence quenching of BNQDs. In this way, a simple 'one-pot' FRET-based biosensor was reported to be constructed to assess AChE activity and its inhibitor by analyzing the fluorescence of BNQDs.
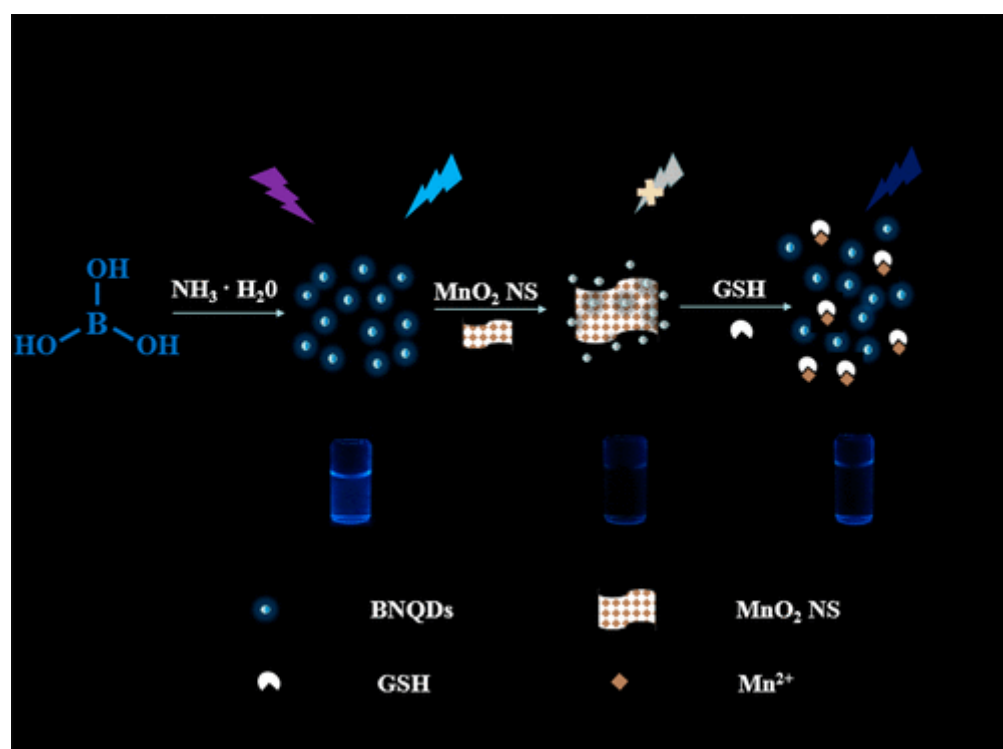
Figure 10. Schematic principle of glutathione (GSH) regulated IFE (inner filter effect) of MnO_2NS on BNQDs for sensing. The observed fluorescence of BNQDs is quenched with the MnO_2NS presence and later recovered with GSH application. Reproduced from [67] with permission from copyright © 2019 American Chemical Society.

4.2. Chemical Sensing

Liu et al. reported the use of BNQDs as fluorescence probes to determine the concentration of ferrous (Fe^{2+}) and ferric (Fe^{3+}) ions with high selectivity, sensitivity, and a low detection limit [64]. For this study, the change in fluorescence intensity with various concentrations of ions (10–600 µM) was investigated at the excitation wavelength of 310 nm. Gradual quenching with increasing concentration resulting in lower fluorescence intensity due to electron transfer from BNQDs to Fe^{2+} and Fe^{3+} ions was reported as seen in Figure 11. The PL quenching efficiency at excitation wavelength 310 nm at various ions concentration showed two linear trends (one for a concentration range of 0–250 µM, and another one for the range of 300–650 µM) for both types of ions. Though the total concentration of both ions can be determined regardless of the oxidation states, detecting individual ions from the mixture is still challenging using this procedure. A similar study for Fe^{3+} detection was reported by Kong et al. [80].

Nickel (Ni^{2+}) ions were reported to be detected in natural water samples via quenching of the fluorescence of BNQDs [79]. Liu et al. reported that the BNQDs prepared in *N*-methyl-2-pyrrolidone (NMP) with green fluorescence were much more competitive than those prepared in ethanol and DMF with blue fluorescence as a competitive fluorescent sensing probe for label-free specific detection of Fe^{3+} or Cu^{2+} [40].
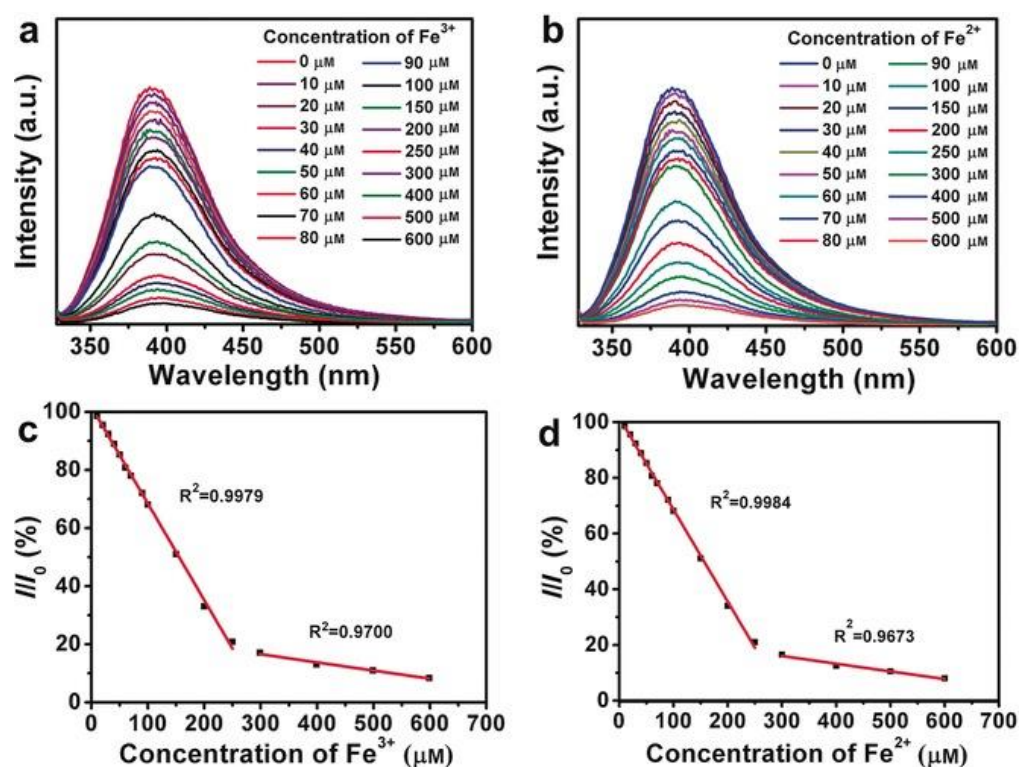
Figure 11. BNQDs-based sensing of (**a**) Fe^{3+} and (**b**) Fe^{2+} by measuring the PL intensity at λ_{ex} = 310 nm, with ion concentrations of 10, 20, 30, 40, 50, 60, 70, 80, 90, 100, 150, 200, 250, 300, 400, 500, and 600 μm, and the linear relationship between the PL-quenching efficiency (I/I_0) at λ_{ex} = 310 nm and the concentration of (**c**) Fe^{3+} and (**d**) Fe^{2+}. Reproduced from [64] with permission from copyright © 2016 Wiley-VCH Verlag GmbH & Co. KGaA (Weinheim, Germany).

Huo et al. [70] reported the strongest fluorescence quenching phenomenon for BNQDs dispersion with Fe^{3+} ions due to the aggregation of BNQDs. There was no obvious fluorescence emission quenching due to other metal ions of the same concentration. This makes BNQDs unique as a selective fluorescence sensing agent for Fe^{3+} ions. In addition to Fe^{3+} ion detection in DI (deionized) water, Dehghani et al. [45] explored the intracellular Fe^{3+} ions detection with the help of non-passivated blue-emitting BNQDs (b-BNQDs). The intercellular detection limit for Fe^{3+} ions was reported as 20.6 nm, which is among the highest sensitivity reported to date. Further, Han et al. [89] reported the fluorescence quenching of BNQDs using Fe^{3+} and Cu^{2+} ions. Interestingly, the fluorescence signals can be switched on and off upon the addition of pyrophosphate (PPi) and alkaline phosphatase (ALP), respectively. The specific detection of PPi and ALP was achievable based on the switch-on and switch-off states of the fluorescence of BNQDs. By comparison of the percentage of fluorescence quenching and recovery of BNQDs, 300 μM Fe^{3+}-mediated fluorescence quenching was found to be more efficient for the sensitive and selective sensing of ALP. The ALP activity measurement was achieved in a linear range between 2 and 200 U L^{-1} with a low limit of detection of 0.8 U L^{-1}. Recently, Yang et al. [78] reported an efficient method to determine tetracyclines (TCs) using ratiometric fluorescence sensors based on BNQDs and europium ion (Eu^{3+}) systems. This system worked as a probe that detected the quenching of blue fluorescence of BNQDs when introduced with TCs, while enhancing the red fluorescence of Eu^{3+}. This phenomenon can be attributed to the inner filter effect, photo-induced electron transfer, and antenna effect. The authors also reported the use of this sensor in the quantitative detection of TCs in milk and beef samples with acceptable recoveries. Further, they developed a test paper for the visual detection of TCs demonstrating the sensor practical application.

4.3. Gas Sensing

Gas sensor fabrication based on BNQDs' decorated zinc oxide (ZnO) nanoplates was reported by Choudhury et al. [69]. These sensors were used for sensing benzene, toluene, ethyl benzene, and xylene (BTEX) vapors. Sensitive sensing of these vapors is important as they are highly toxic and carcinogenic. The sensing response of these ZnO-BNQDs was enhanced greatly as compared to pure ZnO. The X-ray Photoelectron Spectroscopy (XPS) study on this BNQDs-ZnO composite showed that BNQDs are electrically interacted with ZnO via the oxygen atoms and acted as the catalysts for generating charge carriers. The increase in the number of oxygen species decides the sensing capabilities of the composites. This resistance-based gas sensor is based on the variation of conductance resulting from the chemisorption of oxygen molecules on the surface of the sensor. When the gas molecules of BTEX are adsorbed on the sensor surface, they react with the ionized oxygen and lead to oxidation decomposition of BTEX molecules, resulting in electron transfer to the sensor. An optimal temperature of 370 °C was used for the concentration-dependent studies. The response and recovery time of the sensor were reported within 20 s and had good stability.

4.4. Temperature Sensing

Li et al. utilize the variation of PL spectrum intensities of BNQDs with the temperature change as the working principle of temperature sensors [84]. They reported that PL intensities decrease linearly with the increase in temperature from 80 to 440 K when excited at 394 nm, thus making portable non-contact temperature sensors by using BNQDs. The decrease in PL intensity with the increase in temperature is due to the increase in the thermally active nonradiative relaxation process. The PL intensity is reported to be thermally activated with an activation energy of 83.9 meV and has good reversibility. The authors also reported the effect of the size of BNQDs on the sensitivity of the sensor. The relative sensitivity of the sensor with 17.7 nm BNQDs reached the maximum of 0.45 % K^{-1} at 440 K as compared to 0.73% K^{-1} at 440 K with 4.6 nm BNQDs. The relative sensitivity of the sensor based on 4.6 nm BNQDs is better than other materials such as Manganese (Mn), Zinc oxide (ZnO), Erbium (Er), and Ytterbium (Yb)-based sensors reported so far [90–92]. Besides, the sensors based on BNQDs exhibit the widest temperature detection range as compared with other noncontact temperature sensors based on silver nanoclusters, cadmium telluride (CdTe), Zinc sulfide (ZnS), and carbon QDs, as reported in [93–97].

4.5. Fluorescent Staining

Cotton fibers stained with BNQDs were reported to show the excitation wavelength-dependent fluorescence. These fibers emit green and red fluorescence when exposed to blue (450−480 nm) and green (510−550 nm) excitation light, respectively, as shown in Figure 12. This work demonstrated that BNQDs are potential fluorochromes for chemical staining [70]. A similar study was reported later on cotton and silk fibers [40].
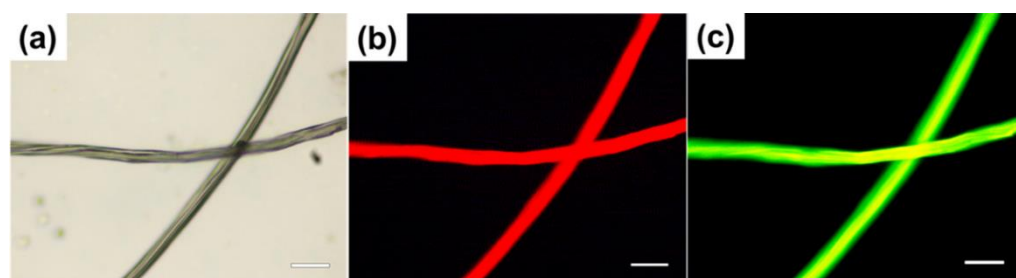

Figure 12. (**a**) Bright-field image of cotton fibers stained with BNQDs. (**b**) Fluorescence image of cotton fibers stained with BNQDs obtained at the excitation wavelengths of 510–550 nm. (**c**) Fluorescence image of cotton fibers stained with BNQDs obtained at the excitation wavelengths of 450–480 nm. Scale bar: 50 μm. Reproduced from [70] with permission from copyright © 2017 American Chemical Society.

4.6. Electrochemiluminescence (ECL) Responses

ECL is luminescence produced by the electrochemical process where a species gener-ated at the electrodes undergo electron transfer reactions to form excited states and emit light. This is a means to convert electrical energy into light energy without the use of excitation light. The ECL mechanism could enable an analytical tool for clinical detection. For example, the ELC of Ruthenium(II) Tris(2,2′-bipyridyl) (Ru(bpy)$_3^{2+}$) and its derivatives-based was demonstrated with excellent efficiency [98]. ECL was also applied in commercial instruments for immunoassays and DNA analyses with high sensitivity and selectivity [99]. For enhanced ECL performance, a suitable co-reactant is needed.

BNQDs, having excellent chemical inertness, exhibit low toxicity and can be used as the alternative ECL luminophores. The ECL property of BNQDs was first reported by Liu et al. [40] using L-cysteine (RSH) as a co-reactant. As shown in Figure 13A, BNQDs displayed ECL emission at an electrode potential of −1.91 V. Adding RSH as the co-reactant, the ECL intensity increased almost five times. ECL was not detected with RSH alone without BNQDs. The reported ECL mechanism is illustrated in Figure 13B. As shown, oxidation of RSH produces free radical intermediates including RS, RSO, RSO$_2$, and RSO$_3$, which reacted with the electron-rich BNQDs (electron transferred from Pt electrode to BNQDs). BNQDs were excited after such electron transfers and emitted measurable luminescent signals. The effect of buffer pH on the ECL behavior was reported. It was shown that the ECL intensity increase with the increase in the buffer pH from 3 to 7, and then decreases when the pH increased over 7, as summarized in Figure 13C. Figure 13D shows the ECL emission of BNQDs with RSH under continuous 14 cyclic Volta metric sweeping with good repeatedly [40].
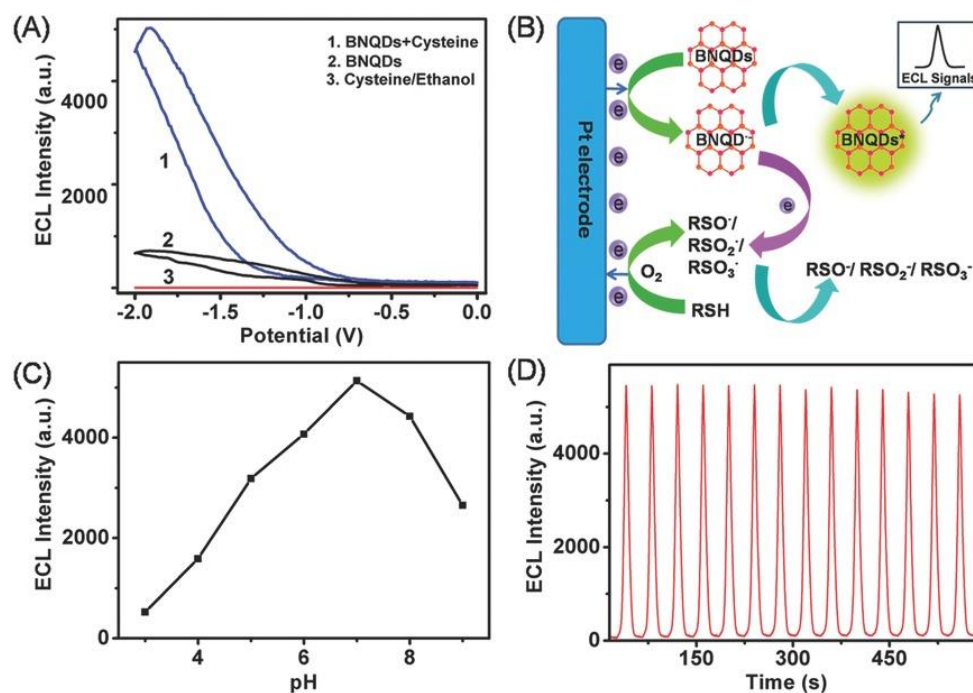

Figure 13. (**A**) Electrochemiluminescence (ECL) intensity–potential curves of 100 mg mL^{-1} BNQDs prepared in ethanol in 100×10^{-3} m PBS (pH 7.0) with varying condition. (**B**) Schematic illustration of the ECL mechanism of the BNQDs/L-cysteine (RSH) system. (**C**) Influences of buffer pH on the ECL intensity of 100 mg mL^{-1} BNQDs. (**D**) ECL intensity–time curve under continuous cyclic voltammetry scanning between −2.0 and 0 V for 600 s for the BNQDs/RSH system. The scan rate is 100 mV s^{-1}. Reproduced from [40] with permission from 2016 Wiley-VCH Verlag GmbH & Co. KGaA (Weinheim, Germany).

Later, Xing et al. [65] reported an enhanced and stable anodic ECL from a suspension of BNQDs and $Ru(bpy)_3^{2+}$, which had a 400-fold enhancement compared with individual $Ru(bpy)_3^{2+}$. BNQDs functionalized with amino groups and the electrocatalytic effect made them efficient co-reactants of $Ru(bpy)_3^{2+}$. The effect of atmosphere and electrode materials on ECL performance was reported. For example, ECL intensity under saturated nitrogen was reported to be higher than that obtained in the air and oxygen atmosphere. The use of glassy carbon electrode yielded better ECL intensity as compared with gold and platinum electrodes. Although tripropylamine (TPA) was shown to be the better co-reactant, BNQDs are the better choice for their better solubility, chemical stability, biocompatibility, and ease of synthesis. Further, ECL sensing for dopamine (DA) was reported based on the quenching effect between the excited state of $Ru(bpy)_3^{2+}$ and the oxidation form of DA in the ECL system of $Ru(bpy)_3^{2+}$/BNQDs [65]. In another study, BNQDs were used as the co-reactants in label-free ECL immune-sensors. Such sensors are based on antigen–antibody interaction for alpha-fetoprotein (AFP) detection in human serum as reported by Qin et al. [68]. The authors integrated $Ru(bpy)_3^{2+}$-doped silica nanoparticles (Ru-SiO$_2$) and AuNP–modified graphene oxide (rGO@Au) to form a rGO@Au@Ru-SiO$_2$ composite which was used as the ECL probe of the sensors. The anode ECL intensity of this composite on GCE was low, but the addition of BNQDs enhanced the ECL intensity by about 100 times. The ECL immuno-sensor was applied for quantitative detection of AFP antigen as ECL signal decreased with the increase in AFP concentration from 0.0001 to 100 ng mL^{-1}. This immune sensor exhibited a low detection limit, high selectivity and sensitivity, acceptable stability, and a wide linear detection range.

The emission spectrum of BNQDs is perfectly matched with the absorption spectrum of nitrogen-doped graphene QDs (NGQDs). Based on this property, Li et al. have demonstrated folic acid (FA) sensors with good selectivity and high recoveries based on ECL resonance energy transfer (ECL-RET) between BNQDs and NGQDs in the presence of co-reactant $K_2S_2O_8$ [66]. The intermediate state of $K_2S_2O_8$, SO_4^{2-}, oxidizes FA and decreases the NGQDs/BNQDs/$K_2S_2O_8$ ECL signal, resulting in the signal-off detection of FA. The ECL intensity of NGQDs by RET was improved by about 10-fold by the addition of BNQDs. This reported method has an advantage against other reported ECL-RET-based sensors [100–103] that use toxic heavy metal QDs that cause serious health and environmental concerns.

Another study by Liu et al. demonstrated the use of BNQDs and gold nanoparticles (AuNPs) as biosensors to accurately quantify the Shiga toxin-producing Escherichia Coli gene from 1 pmol L^{-1} to 5 nmol L^{-1} with a limit of detection of 0.3 pmol L^{-1} [74]. This biosensor can be used for DNA detection and was designed based on the ECL-RET principle, and surface plasmon coupling (SPC) effects between AuNPs and BNQDs. In brief, a hairpin DNA probe was made by binding BNQDs and AuNPs to its end. The ECL signal of the BNQDs was quenched by the AuNPs due to ECL-RET between the AuNPs and BNQDs. When the hairpin DNA probe identified the target DNA, the distance between BNQDs and AuNPs increased due to the linear transformation of the hairpin structure. As a result, the SPC-ECL effect suppressed the ECL-RET effect, thus enhancing the ECL signal (due to coupling of light emission with surface plasmon resonance) by about six times higher than BNQDs-Au NPs- hairpin DNA conjugates. The authors further reported on the use of S-regulated BNQDs along with AuNPs with higher ECL performance for BRAF gene detection and quantification using the same SPC-ECL strategy as discussed above [75]. Further, Liang et al. [104] reported the first polarized-ECL biosensor developed using SPC-ECL strategy and fluorine-doped BNQDs to detect the K-ras gene. The fluorine-doped BNQDs ECL signal was reported to be enhanced at a specific polarization angle, thanks to polarization angle-dependent SPC-ECL. This polarized-biosensor was reported to quantify the K-ras gene from 0.1 fM to 10 nM, with the detection limit as 0.03 fM.

Recently, Wang et al. [105] reported the construction of ECL biosensor using BNQDs as a co-reactant of luminol for the quantitative determination of concanavalin A (Con A). BNQDs are used for boosting the ECL intensity of luminol, almost producing a 10-fold

enhancement as compared with single poly (luminol/aniline) nanorods loaded on reduced graphene oxide using GCE. The detection limit of Con A was reported in the range of 1.0 pgmL^{-1} to 1.0 µgmL^{-1} with a low detection limit of 0.15 pgmL^{-1}.

4.7. Photocatalyst

Radhakrishnan et al. reported the use of TiO_2 nanotubes/FBNQDs heterojunctions as the broad-spectrum photocatalyst for efficient water splitting [58]. Hydrogen production enhancement was reported when FBNQDs were loaded on TiO_2 nanotubes (NT). This was demonstrated by using photoelectrochemical cells consisting of the platinum cathode, and TiO_2 nanotubes/FBNQDs photoanode, where visible light from solar radiation was used to generate hydrogen and oxygen from water. A hydrogen production conversion efficiency of up to 24% was obtained after adding FBNQDs onto TiO_2 nanotubes, paving an alternative way in the design of efficient visible-light photocatalysts. Later, Yang et al. reported metal-free heterostructure photocatalyst using ultrathin porous graphitic carbon nitride (UPCN) decorated with BNQDs [71]. The use of BNQDs has promoted the dissociation of excitons and accelerated the transfer of charges. This BNQDs/UPCN (BU) photocatalyst used visible light to degrade oxytetracycline hydrochloride (OTC−HCl) for molecular oxygen activation by the generation of superoxide radical (O_2^-). Further, BU photocatalyst along with visible light irradiation was used to produce hydrogen peroxide (H_2O_2) from the mixture of IPA and deionized water. The average O_2^- generation rate for the best-optimized sample was about 2.3 and 1.6 times better than that of bulk graphitic carbon nitride (g-C_3N_4) and UPCN, respectively. Moreover, the H_2O_2 production by the same sample was 3.2 and 2 times higher than that of bulk g-C_3N_4 and UPCN, respectively, for 60 min.

The incorporation of BNQDs to tungsten trioxide (WO_3) photoanode was reported for efficient photogenerated charge separation, and charge recombination for the photoelectrochemical (PEC) water splitting application [72]. It was thought that BNQDs help to extract the photogenerated holes, thus enhancing charge separation and water oxidation potency. A 2.4-fold enhancement in photocurrent density and 2.44-fold enhancement in charge carrier density were reported by using such BNQD-modified photoanode in comparison to the pristine WO_3 anode. Moreover, the incident photon to current conversion efficiency (IPCE) using the modified photoanode has reached 32%, which is 2.1 times higher than that when pristine WO_3 anode was used. On the other hand, Sahu et al. reported superior PEC performance in water splitting using BNQDs incorporated over fluorine-doped hematite (F-Fe_2O_3) nanorods [73]. 1-D hematite nanorod arrays quickly transferred electrons to the FTO substrate, while BNQDs acted as the efficient hole extractors that enhanced charge separation on the hematite surface by decreasing the hole trapping probability. In the optimal condition, a carrier density of 2.08×10^{20} cm^{-3} was obtained, which is two orders of magnitude higher than that when bare α-Fe_2O_3 photoanode was used. This resulted in a photocurrent density of 2.24 mA cm^{-2} at 1.23 V, which is six-fold higher than the case when bare hematite was used. The faradaic efficiency test of F-Fe_2O_3-BNQDs for oxygen evolution was reported to be 90% after 1 h of irradiation, confirming that most of the photo-generated charges were utilized for water oxidation.

4.8. Other Applications

Because of the low shielding effect of the h-BN planes in proton transport [106], BN-QDs suspended in water were investigated for their roles in proton exchange membranes (PEMs) by Lei et al. [39]. The authors reported easy integration of BNQDs into polymer matrix resulting in enhanced thermal stability and proton conductivities of the composite PEMs with an enhanced water retention capability.

With the electronic devices getting smaller and smaller with high integration and power density, dissipating heat effectively is highly desirable for ensuring their long life-time and reliability. The good thermal conductivity and excellent electrical insulation in h-BN materials make them a good candidate for thermal management applications. BN

nanosheets were added into the polymer matrix as filler to form effective thermal conductive paths that significantly improve the thermal conductivity of the composites [107–114]. Theoretical studies on thermoelectric properties of BNQDs were conducted to inspire experimentalists to seek ways for real-world applications [3]. For example, Zhou et al. [115] reported the doping of BNQDs on a flexible polyamide-imide (PAI)/BN nanosheets composite film to improve the thermal conductivity (TC) of the polymer and track the thermal conductive paths utilizing the photoluminescence (PL) of BNQDs. In this case, BNQDs were filled into the gaps between the BN nanosheet fillers and the polymer matrix, forming the continuous thermal conductive paths. For low filler content (BN nanosheets 9% wt) and 1% wt BNQDs, the hybrid composite film resulted in an in-plane TC of 7.69 W m^{-1} K^{-1} and had good optical transparency, making it a possible candidate for use as a flexible display substrate.

The use of BNQDs as readout labels for logic gate construction was first reported by Han et al. [89] based on the principle of signal-on and -off in the BNQDs-Fe^{3+} FL in the PPi and ALP assays. The existence of PPi and ALP was used as the inputs ("1" state for present and "0" state for absence). The normalized FL intensity of BNQDs under optimal excitation conditions was used as the output signal. The reported application for inhibiting "INH" logic gate construction could pave a path for the use of other 2D-QDs for a future logic gate design.

Beytur [116] reported the use of BNQDs in preparation for Platinum nanoparticle (PtNPs)/BNQDs/6-methyl-2-(3-hydroxy-4-methoxybenzylidenamino)-benzothiazole(ILs) nanocomposite (PtNPs/BNQDs/ILs) for the electrocatalytic oxidation of methanol. The performance of this nanocomposite was better than while using only ILs and BNQDs/ILs.

5. Conclusions

Since the successful synthesis in 2014, BNQDs have gained considerable attention for their photochemical properties, photostability, and biocompatibility. All the publications so far have shown that the synthetic route is simple and cost-efficient; however, more creativity to scale-up the production efficiency is needed for the large-scale and real-world application of BNQDs. There is no doubt that BNQDs have already shown immense potential in sensors, bioimaging, phototherapy, photocatalysis, and biomedicine. We are expected to see creativity in the use of BNQDs for many other applications, for example, based on the edge functionalization of these van der Walls nanostructures, and solar energy harvesting based on the broad light absorption nature of the QDs. All these will rely on the high-yield synthesis of BNQDs with controllable sizes. Breakthrough in large-scale synthesis and real-world application will promote the future science, engineering, and application of BNQDs.

References

1. Zhi, C.; Xu, Y.; Bando, Y.; Golberg, D. Highly thermo-conductive fluid with boron nitride nanofillers. *ACS Nano* **2011**, *5*, 6571–6577. [CrossRef] [PubMed]
2. Li, L.H.; Santos, E.J.G.; Xing, T.; Cappelluti, E.; Roldán, R.; Chen, Y.; Watanabe, K.; Taniguchi, T. Dielectric screening in atomically thin boron nitride nanosheets. *Nano Lett.* **2014**, *15*, 218–223. [CrossRef] [PubMed]

3. Pan, C.; Long, M.; He, J. Enhanced thermoelectric properties in boron nitride quantum-dot. *Results Phys.* **2017**, *7*, 1487–1491. [CrossRef]

4. Lee, C.H.; Xie, M.; Kayastha, V.; Wang, J.; Yap, Y.K. Patterned growth of boron nitride nanotubes by catalytic chemical vapor deposition. *Chem. Mater.* **2010**, *22*, 1782–1787. [CrossRef]

5. Qin, J.-K.; Liao, P.-Y.; Si, M.; Gao, S.; Qiu, G.; Jian, J.; Wang, Q.; Zhang, S.-Q.; Huang, S.; Charnas, A.; et al. Raman response and transport properties of tellurium atomic chains encapsulated in nanotubes. *Nat. Electron.* **2020**, *3*, 141–147. [CrossRef]

6. Bhandari, S.; Hao, B.; Waters, K.; Lee, C.H.; Idrobo, J.C.; Zhang, D.; Pandey, R.; Yap, Y.K. Two-dimensional gold quantum dots with tunable bandgaps. *ACS Nano* **2019**, *13*, 4347–4353. [CrossRef] [PubMed]

7. Lee, C.H.; Bhandari, S.; Tiwari, B.; Yapici, N.; Zhang, D.; Yap, Y.K. Boron nitride nanotubes: Recent advances in their synthesis, functionalization, and applications. *Molecules* **2016**, *21*, 922. [CrossRef]

8. Lee, C.H.; Qin, S.; Savaikar, M.A.; Wang, J.; Hao, B.; Zhang, D.; Banyai, D.; Jaszczak, J.A.; Clark, K.W.; Idrobo, J.-C.; et al. Room-temperature tunneling behavior of boron nitride nanotubes functionalized with gold quantum dots. *Adv. Mater.* **2013**, *25*, 4544–4548. [CrossRef] [PubMed]

9. Wang, J.; Lee, C.H.; Yap, Y.K. Recent advancements in boron nitride nanotubes. *Nanoscale* **2010**, *2*, 2028–2034. [CrossRef]

10. Iijima, S. Helical microtubules of graphitic carbon. *Nat. Cell Biol.* **1991**, *354*, 56–58. [CrossRef]

11. Novoselov, K.S.; Geim, A.K.; Morozov, S.V.; Jiang, D.; Zhang, Y.; Dubonos, S.V.; Grigorieva, I.V.; Firsov, A.A. Electric field effect in atomically thin carbon films. *Science* **2004**, *306*, 666–669. [CrossRef]

12. Geim, A.K.; Grigorieva, I.V. Van der Waals heterostructures. *Nat. Cell Biol.* **2013**, *499*, 419–425. [CrossRef]

13. Luo, W.; Wang, Y.; Hitz, E.; Lin, Y.; Yang, B.; Hu, L. Solution processed boron nitride nanosheets: Synthesis, assemblies and emerging applications. *Adv. Funct. Mater.* **2017**, *27*, 1701450. [CrossRef]

14. Coleman, J.N.; Lotya, M.; O'Neill, A.; Bergin, S.D.; King, P.J.; Khan, U.; Young, K.; Gaucher, A.; De, S.; Smith, R.J.; et al. Two-dimensional nanosheets produced by liquid exfoliation of layered materials. *Science* **2011**, *331*, 568–571. [CrossRef] [PubMed]

15. Nakamura, J.; Nitta, T.; Natori, A. Electronic and magnetic properties of BNC ribbons. *Phys. Rev. B* **2005**, *72*, 205429. [CrossRef]

16. Zheng, F.; Zhou, G.; Liu, Z.; Wu, J.; Duan, W.; Gu, B.L.; Zhang, S.B. Half metallicity along the edge of zigzag boron Ni-tride nanoribbons. *Phys. Rev. B Condens. Matter Mater. Phys.* **2008**, *78*, 205415. [CrossRef]

17. Barone, V.; Peralta, J.E. Magnetic boron nitride nanoribbons with tunable electronic properties. *Nano Lett.* **2008**, *8*, 2210–2214. [CrossRef] [PubMed]

18. Zhang, Z.; Guo, W. Energy-gap modulation of BN ribbons by transverse electric fields: First-principles calculations. *Phys. Rev. B* **2008**, *77*, 075403. [CrossRef]

19. Xi, Y.; Zhao, M.; Wang, X.; Li, S.; He, X.; Wang, Z.; Bu, H. Honeycomb-patterned quantum dots beyond graphene. *J. Phys. Chem. C* **2011**, *115*, 17743–17749. [CrossRef]

20. Bandyopadhyay, A.; Sharma, S.R.K.C.Y.; Pati, S.K. Tuning the electronic and optical properties of graphene and Boron nitride quantum dots by molecular charge-transfer interactions: A theoretical study. *Phys. Chem. Chem. Phys.* **2013**, *15*, 13881–13887. [CrossRef] [PubMed]

21. Yamijala, S.S.; Bandyopadhyay, A.; Pati, S.K. Structural stability, electronic, magnetic, and optical properties of rectangular graphene and boron nitride quantum dots: Effects of size, substitution, and electric field. *J. Phys. Chem. C* **2013**, *117*, 23295–23304. [CrossRef]

22. Stengl, V.; Kormunda, M.; Štengl, V.; Henych, J. Self-assembled BN and BCN quantum dots obtained from high intensity ultrasound exfoliated nanosheets. *Sci. Adv. Mater.* **2014**, *6*, 1–11. [CrossRef]

23. Lin, L.; Xu, Y.; Zhang, S.; Ross, I.M.; Ong, A.C.M.; Allwood, D.A. Fabrication and luminescence of monolayered boron nitride quantum dots. *Small* **2013**, *10*, 60–65. [CrossRef] [PubMed]

24. Shtansky, D.V.; Firestein, K.L.; Golberg, D.V. Fabrication and application of BN nanoparticles, nanosheets and their nanohybrids. *Nanoscale* **2018**, *10*, 17477–17493. [CrossRef]

25. Stagi, L.; Ren, J.; Innocenzi, P. From 2-D to 0-D boron nitride materials, the next challenge. *Materials* **2019**, *12*, 3905. [CrossRef]

26. Paine, R.T.; Narula, C.K. Synthetic routes to boron nitride. *Chem. Rev.* **1990**, *90*, 73–91. [CrossRef]

27. Mishra, N.S.; Saravanan, P. A review on the synergistic features of hexagonal boron nitride (white graphene) as Ad-sorbent-photo active nanomaterial. *Chem. Select* **2018**, *3*, 8023–8034.

28. Zhang, W.J.; Chong, Y.M.; Bello, I.; Lee, S.T. Nucleation, growth and characterization of cubic boron nitride (cBN) films. *J. Phys. D Appl. Phys.* **2007**, *40*, 6159–6174. [CrossRef]

29. Lee, C.H.; Kayastha, V.K.; Wang, J.; Yap, Y.K. Introduction to B-C-N materials. In *B-C-N Nanotubes and Related Nanostructures*; Springer: New York, NY, USA, 2009; Volume 6, pp. 1–22. [CrossRef]

30. Hao, B.; Lee, C.H.; Wang, J.; Asthana, A.; Winslow, D.; Zhang, D.; Yap, Y.K. Controlled synthesis of functional boron nitride nanostructures for applications. In *Nanotubes and Nanosheets: Functionalization and Applications of Boron Nitride and Other Materials*; Ying, I.C., Ed.; CRC Press: Boca Raton, FL, USA, 2015; pp. 551–572.

31. Bhandari, S.; Tiwari, B.; Yapici, N.; Zhang, N.; Yap, Y.K. Introduction to boron nitride nanotubes: Synthesis, properties, functionalization, and cutting. In *Boron Nitride Nanotubes in Nanomedicine*; Elsevier: Amsterdam, The Netherlands, 2016; pp. 1–15. Available online: https://www.sciencedirect.com/science/article/pii/B9780323389457000018 (accessed on 26 March 2021).

32. Hod, O. Graphite and hexagonal boron-nitride have the same interlayer distance. Why? *J. Chem. Theory Comput.* **2012**, *8*, 1360–1369. [CrossRef]

33. Gorbachev, R.V.; Riaz, I.; Nair, R.R.; Jalil, R.; Britnell, L.; Belle, B.D.; Hill, E.W.; Novoselov, K.S.; Watanabe, K.; Taniguchi, T.; et al. Hunting for monolayer boron nitride: Optical and Raman signatures. *Small* **2011**, *7*, 465–468. [CrossRef]

34. Paciĺ, D.; Meyer, J.C.; Girit, Ç.; Zettl, A. The two-dimensional phase of boron nitride: Few-atomic-layer sheets and suspended membranes. *Appl. Phys. Lett.* **2008**, *92*, 133107. [CrossRef]

35. Wu, S.; Brzozowski, K.J. Surface free energy and polarity of organic pigments. *J. Colloid Interface Sci.* **1971**, *37*, 686–690. [CrossRef]

36. Li, H.; Tay, R.Y.; Tsang, S.H.; Zhen, X.; Teo, E.H.T. Controllable synthesis of highly luminescent boron nitride quantum dots. *Small* **2015**, *11*, 6491–6499. [CrossRef] [PubMed]

37. Zhu, S.; Zhang, J.; Qiao, C.; Tang, S.; Li, Y.; Yuan, W.; Li, B.; Tian, L.; Liu, F.; Hu, R.; et al. Strongly green-photoluminescent graphene quantum dots for bioimaging applications. *Chem. Commun.* **2011**, *47*, 6858–6860. [CrossRef] [PubMed]

38. Shen, J.; Zhu, Y.; Yang, X.; Zong, J.; Zhang, J.; Li, C. One-pot hydrothermal synthesis of graphene quantum dots sur-face-passivated by polyethylene glycol and their photoelectric conversion under near-infrared light. *N. J. Chem.* **2012**, *36*, 97–101. [CrossRef]

39. Lei, Z.; Xu, S.; Wan, J.; Wu, P. Facile preparation and multifunctional applications of boron nitride quantum dots. *Nanoscale* **2015**, *7*, 18902–18907. [CrossRef]

40. Liu, M.; Xu, Y.; Wang, Y.; Chen, X.; Ji, X.; Niu, F.; Song, Z.; Liu, J. Boron nitride quantum dots with solvent-regulated blue/green photoluminescence and electrochemiluminescent behavior for versatile applications. *Adv. Opt. Mater.* **2017**, *5*, 1600661. [CrossRef]

41. Yola, M.L.; Atar, N. Development of cardiac troponin-I biosensor based on boron nitride quantum dots including molecularly imprinted polymer. *Biosens. Bioelectron.* **2019**, *126*, 418–424. [CrossRef]

42. Fan, L.; Zhou, Y.; He, M.; Tong, Y.; Zhong, X.; Fang, J.; Bu, X. Facile microwave approach to controllable boron nitride quantum dots. *J. Mater. Sci.* **2017**, *52*, 13522–13532. [CrossRef]

43. Kumar, R.; Singh, R.K.; Yadav, S.K.; Savu, R.; Moshkalev, S.A. Mechanical pressure-induced chemical cutting of boron nitride sheets into boron nitride quantum dots and optical properties. *J. Alloys Compd.* **2016**, *683*, 38–45. [CrossRef]

44. Xue, Q.; Zhang, H.; Zhu, M.; Wang, Z.; Pei, Z.; Huang, Y.; Song, X.; Zeng, H.; Zhi, C. Hydrothermal synthesis of blue-fluorescent monolayer BN and BCNO quantum dots for bio-imaging probes. *RSC Adv.* **2016**, *6*, 79090–79094. [CrossRef]

45. Dehghani, A.; Ardekani, S.M.; Lesani, P.; Hassan, M.; Gomes, V.G. Two-photon active boron nitride quantum dots for multiplexed imaging, intracellular ferric ion biosensing, and pH tracking in living cells. *ACS Appl. Bio Mater.* **2018**, *1*, 975–984. [CrossRef]

46. Liu, Q.; Hu, C.; Wang, X. One-pot solvothermal synthesis of water-soluble boron nitride nanosheets and fluorescent boron nitride quantum dots. *Mater. Lett.* **2019**, *234*, 306–310. [CrossRef]

47. Jung, J.-H.; Kotal, M.; Jang, M.-H.; Lee, J.; Cho, Y.-H.; Kim, W.-J.; Oh, I.-K. Defect engineering route to boron nitride quantum dots and edge-hydroxylated functionalization for bio-imaging. *RSC Adv.* **2016**, *6*, 73939–73946. [CrossRef]

48. Lin, L.; Zhang, S. Creating high yield water-soluble luminescent graphene quantum dots via exfoliating and disintegrating carbon nanotubes and graphite flakes. *Chem. Commun.* **2012**, *48*, 10177–10179. [CrossRef]

49. Peng, D.; Zhang, L.; Li, F.F.; Cui, W.R.; Liang, R.P.; Qiu, J.D. Facile and green approach to the synthesis of boron Ni-tride quantum dots for 2,4,6-trinitrophenol sensing. *ACS Appl. Mater. Interfaces* **2018**, *10*, 7315–7323. [CrossRef]

50. Thangasamy, P.; Santhanam, M.; Sathish, M. Supercritical fluid facilitated disintegration of hexagonal boron nitride nanosheets to quantum dots and its application in cells imaging. *ACS Appl. Mater. Interfaces* **2016**, *8*, 18647–18651. [CrossRef] [PubMed]

51. Rangappa, D.; Sone, K.; Wang, M.; Gautam, U.K.; Golberg, D.; Itoh, H.; Ichihara, M.; Honma, I. Rapid and direct conversion of graphite crystals into high-yielding, good-quality graphene by supercritical fluid exfoliation. *Chem. A Eur. J.* **2010**, *16*, 6488–6494. [CrossRef]

52. Thangasamy, P.; Sathish, M. Supercritical fluid processing: A rapid, one-pot exfoliation process for the production of surfactant-free hexagonal boron nitride nanosheets. *CrystEngComm* **2015**, *17*, 5895–5899. [CrossRef]

53. Sathish, M.; Mitani, S.; Tomai, T.; Honma, I. Supercritical fluid assisted synthesis of N-doped graphene nanosheets and their capacitance behavior in ionic liquid and aqueous electrolytes. *J. Mater. Chem. A* **2014**, *2*, 4731–4738. [CrossRef]

54. Thangasamy, P.; Sathish, M. Rapid, one-pot synthesis of luminescent MoS2 nanoscrolls using supercritical fluid processing. *J. Mater. Chem. C* **2016**, *4*, 1165–1169. [CrossRef]

55. Angizi, S.; Hatamie, A.; Ghanbari, H.; Simchi, A.A. Mechanochemical green synthesis of exfoliated edge-functionalized boron nitride quantum dots: Application to vitamin C sensing through hybridization with gold electrodes. *ACS Appl. Mater. Interfaces* **2018**, *10*, 28819–28827. [CrossRef]

56. Angizi, S.; Shayeganfar, F.; Azar, M.H.; Simchi, A. Surface/edge functionalized boron nitride quantum dots: Spectroscopic fingerprint of bandgap modification by chemical functionalization. *Ceram. Int.* **2020**, *46*, 978–985. [CrossRef]

57. Cai, R.; Nie, M.; Xu, F. Ultrafast turbulence-induced disintegration of BN and WS2 quantum dots for potential multifunctional nanotheranostics. *Mater. Des.* **2019**, *181*, 107925. [CrossRef]

58. Radhakrishnan, S.; Park, J.H.; Neupane, R.; Reyes, C.A.D.L.; Sudeep, P.M.; Paulose, M.; Martí, A.A.; Tiwary, C.S.; Khabashesku, V.N.; Varghese, O.K.; et al. Fluorinated boron nitride quantum dots: A new 0D material for energy conversion and detection of cellular metabolism. *Part. Part. Syst. Charact.* **2019**, *36*, 1800346. [CrossRef]

59. Duong, N.M.H.; Glushkov, E.; Chernev, A.; Navikas, V.; Comtet, J.; Nguyen, M.A.P.; Toth, M.; Radenovic, A.; Tran, T.T.; Aharonovich, I. Facile production of hexagonal boron nitride nanoparticles by cryogenic exfoliation. *Nano Lett.* **2019**, *19*, 5417–5422. [CrossRef] [PubMed]

60. Matveev, A.T.; Firestein, K.L.; Steinman, A.E.; Kovalskii, A.M.; Sukhorukova, I.V.; Lebedev, O.I.; Shtansky, D.V.; Golberg, D. Synthesis of boron nitride nanostructures from borates of alkali and alkaline earth metals. *J. Mater. Chem. A* **2015**, *3*, 20749–20757. [CrossRef]

61. Weng, Q.; Ide, Y.; Wang, X.; Wang, X.; Zhang, C.; Jiang, X.; Xue, Y.; Dai, P.; Komaguchi, K.; Bando, Y.; et al. Design of BN porous sheets with richly exposed (002) plane edges and their application as TiO2 visible light sensitizer. *Nano Energy* **2015**, *16*, 19–27. [CrossRef]

62. Xiong, C.; Tu, W. Synthesis of water-dispersible boron nitride nanoparticles. *Eur. J. Inorg. Chem.* **2014**, *2014*, 3010–3015. [CrossRef]

63. Wang, L.; Wu, B.; Jiang, L.; Chen, J.; Li, Y.; Guo, W.; Hu, P.; Liu, Y. Growth and etching of monolayer hexagonal boron nitride. *Adv. Mater.* **2015**, *27*, 4858–4864. [CrossRef] [PubMed]

64. Liu, B.; Yan, S.; Song, Z.; Liu, M.; Ji, X.; Yang, W.; Liu, J. One-step synthesis of boron nitride quantum Dots: Simple chemistry meets delicate nanotechnology. *Chem. A Eur. J.* **2016**, *22*, 18899–18907. [CrossRef]

65. Xing, H.; Zhai, Q.; Zhang, X.; Li, J.; Wang, E. Boron nitride quantum dots as efficient coreactant for enhanced electrochemiluminescence of ruthenium(II) Tris(2,2′-Bipyridyl). *Anal. Chem.* **2018**, *90*, 2141–2147. [CrossRef] [PubMed]

66. Li, M.; Wang, C.; Chen, L.; Liu, D. A novel electrochemiluminescence sensor based on resonance energy transfer system between nitrogen doped graphene quantum dots and boron nitride quantum dots for sensitive detection of folic acid. *Anal. Chim. Acta* **2019**, *1090*, 57–63. [CrossRef]

67. Peng, C.; Xing, H.; Fan, X.; Xue, Y.; Li, J.; Wang, E. Glutathione regulated inner filter effect of MnO 2 nanosheets on boron nitride quantum dots for sensitive assay. *Anal. Chem.* **2019**, *91*, 5762–5767. [CrossRef]

68. Qin, D.; Jiang, X.; Mo, G.; Feng, J.; Deng, B. Boron nitride quantum dots as electrochemiluminescence coreactants of RGO@Au@Ru–SiO2 for label-free detection of AFP in human serum. *Electrochim. Acta* **2020**, *335*, 135621. [CrossRef]

69. Choudhury, S.P.; Feng, Z.; Gao, C.; Ma, X.; Zhan, J.; Jia, F. BN quantum dots decorated ZnO nanoplates sensor for enhanced detection of BTEX gases. *J. Alloys Compd.* **2020**, *815*, 152376. [CrossRef]

70. Huo, B.; Liu, B.; Chen, T.; Cui, L.; Xu, G.; Liu, M.; Liu, J. One step synthesis of fluorescent boron nitride quantum dots via a hydrothermal strategy using melamine as nitrogen source for the detection of ferric ions. *Langmuir* **2017**, *33*, 10673–10678. [CrossRef]

71. Yang, Y.; Zhang, C.; Huang, D.; Zeng, G.; Huang, J.; Lai, C.; Zhou, C.; Wang, W.; Guo, H.; Xue, W.; et al. Boron nitride quantum dots decorated ultrathin porous g-C3N4: Intensified exciton dissociation and charge transfer for promoting visible-light-driven molecular oxygen activation. *Appl. Catal. B Environ.* **2019**, *245*, 87–99. [CrossRef]

72. Mohanta, M.K.; Sahu, T.K.; Gogoi, D.; Peela, N.R.; Qureshi, M. Hexagonal boron nitride quantum dots as a superior hole Extractor for efficient charge separation in WO3-based photoelectrochemical water oxidation. *ACS Appl. Energy Mater.* **2019**, *2*, 7457–7466. [CrossRef]

73. Sahu, T.K.; Mohanta, M.K.; Qureshi, M. Modulating water oxidation kinetics utilizing H-BN quantum dots as an efficient hole extractor on fluorine doped hematite photoanode. *J. Power Sources* **2020**, *445*, 227341. [CrossRef]

74. Liu, Y.; Chen, X.; Wang, M.; Ma, Q. A visual electrochemiluminescence resonance energy transfer/surface plasmon coupled electrochemiluminescence nanosensor for Shiga toxin-producing *Escherichia coli* detection. *Green Chem.* **2018**, *20*, 5520–5527. [CrossRef]

75. Liu, Y.; Wang, M.; Nie, Y.; Zhang, Q.; Ma, Q. Sulfur regulated boron nitride quantum dots electrochemiluminescence with amplified surface plasmon coupling strategy for BRAF gene detection. *Anal. Chem.* **2019**, *91*, 6250–6258. [CrossRef]

76. Yasnó, J.P.; Kiminami, R.H. Short time reaction synthesis of nano-hexagonal boron nitride. *Adv. Powder Technol.* **2020**, *31*, 4436–4443. [CrossRef]

77. Jerome, R.; Sundramoorthy, A.K. Hydrothermal synthesis of boron nitride quantum dots/poly(luminol) nanocomposite for selective detection of ascorbic acid. *J. Electrochem. Soc.* **2019**, *166*, B3017–B3024. [CrossRef]

78. Yang, K.; Jia, P.; Hou, J.; Bu, T.; Sun, X.; Liu, Y.; Wang, L. Innovative dual-emitting ratiometric fluorescence sensor for tetracyclines detection based on boron nitride quantum dots and europium ions. *ACS Sustain. Chem. Eng.* **2020**, *8*, 17185–17193. [CrossRef]

79. Yao, Q.; Feng, Y.; Rong, M.; He, S.; Chen, X. Determination of nickel(II) via quenching of the fluorescence of boron nitride quantum dots. *Microchim. Acta* **2017**, *184*, 4217–4223. [CrossRef]

80. Kong, Y.; He, Y.; Zhou, J.; Zhong, S.; Song, G. Amino acids as the nitrogen source to synthesize boron nitride quantum dots for fluorescence turn-off-on detection of ascorbic acid. *ChemistrySelect* **2020**, *5*, 3828–3834. [CrossRef]

81. Zhao, H.; Ding, J.; Ji, N.; Xu, B.; Yu, H. Boron nitride quantum dots derived from renewable lignin. *ChemistrySelect* **2019**, *4*, 3025–3030. [CrossRef]

82. Wang, X.B.; Weng, Q.; Wang, X.; Li, X.; Zhang, J.; Liu, F.; Jiang, X.F.; Guo, H.; Xu, N.; Golberg, D.; et al. Biomass directed synthesis of 20 g high-quality boron nitride nanosheets for thermoconductive polymeric composites. *ACS Nano* **2014**, *8*, 9081–9088. [CrossRef]

83. Ahmad, P.; Khandaker, M.U.; Muhammad, N.; Khan, G.; Rehman, F.; Khan, A.S.; Ullah, Z.; Khan, A.; Ali, H.; Ahmed, S.M.; et al. Fabrication of hexagonal boron nitride quantum dots via a facile bottom-up technique. *Ceram. Int.* **2019**, *45*, 22765–22768. [CrossRef]

84. Li, Q.; Zheng, Y.; Hou, X.; Yang, T.; Liang, T.; Zheng, J. A wide range photoluminescence intensity based temperature sensor developed with BN quantum dots and the photoluminescence mechanism. *Sens. Actuators B Chem.* **2020**, *304*, 127353. [CrossRef]

85. Lim, S.Y.; Shen, W.; Gao, Z. Carbon quantum dots and their applications. *Chem. Soc. Rev.* **2015**, *44*, 362–381. [CrossRef] [PubMed]

86. Zhao, Y.; Butler, E.B.; Tan, M. Targeting cellular metabolism to improve cancer therapeutics. *Cell Death Dis.* **2013**, *4*, e532. [CrossRef]
87. Yola, M.L. Electrochemical activity enhancement of monodisperse boron nitride quantum dots on graphene oxide: Its application for simultaneous detection of organophosphate pesticides in real samples. *J. Mol. Liq.* **2019**, *277*, 50–57. [CrossRef]
88. Zhan, Y.; Yang, J.; Guo, L.; Luo, F.; Qiu, B.; Hong, G.; Lin, Z. Targets regulated formation of boron nitride quantum dots—Gold nanoparticles nanocomposites for ultrasensitive detection of acetylcholinesterase activity and its inhibitors. *Sens. Actuators B Chem.* **2019**, *279*, 61–68. [CrossRef]
89. Han, Y.; Niu, Y.; Liu, M.; Niu, F.; Xu, Y.; Niu, F. A rational strategy to develop a boron nitride quantum dot-based molecular logic gate and fluorescent assay of alkaline phosphatase activity. *J. Mater. Chem. B* **2019**, *7*, 897–902. [CrossRef]
90. Park, Y.; Koo, C.; Chen, H.Y.; Han, A.; Son, D.H. Ratiometric temperature imaging using environment insensitive luminescence of Mn-doped core shell nanocrystals. *Nanoscale* **2013**, *5*, 4944–4950. [CrossRef]
91. Wang, X.; Kong, X.; Yu, Y.; Sun, Y.; Zhang, H. Effect of annealing on upconversion luminescence of ZnO:Er3+ nano-crystals and high thermal sensitivity. *J. Phys. Chem. C* **2007**, *111*, 15119–15124. [CrossRef]
92. Singh, S.K.; Kumar, K.; Rai, S. Er3+/Yb3+ codoped Gd2O3 nano-phosphor for optical thermometry. *Sens. Actuators A Phys.* **2009**, *149*, 16–20. [CrossRef]
93. Wang, S.; Westcott, S.; Chen, W. Nanoparticle luminescence thermometry. *J. Phys. Chem. B* **2002**, *106*, 11203–11209. [CrossRef]
94. Lan, J.; Zou, H.; Liu, Z.; Gao, M.; Chen, B.; Li, Y.; Huang, C. A visual physiological temperature sensor developed with gelatin-stabilized luminescent silver nanoclusters. *Talanta* **2015**, *143*, 469–473. [CrossRef]
95. Wang, C.; Xu, Z.; Cheng, H.; Lin, H.; Humphrey, M.G.; Zhang, C. A hydrothermal route to water-stable luminescent carbon dots as nanosensors for pH and temperature. *Carbon* **2015**, *82*, 87–95. [CrossRef]
96. Ding, Q.; Zhang, X.; Li, L.; Lou, X.; Xu, J.; Zhou, P.; Yan, M. Temperature dependent photoluminescence of composition tunable Zn_xAgInSe quantum dots and temperature sensor application. *Opt. Express* **2017**, *25*, 19065–19076. [CrossRef]
97. Chen, P.-C.; Chen, Y.-N.; Hsu, P.-C.; Shih, C.-C.; Chang, H.-T. Photoluminescent organosilane-functionalized carbon dots as temperature probes. *Chem. Commun.* **2013**, *49*, 1639–1641. [CrossRef]
98. Zhai, Q.; Li, J.; Wang, E. Recent advances based on nanomaterials as electrochemiluminescence probes for the fabrication of sensors. *Chem Electro Chem* **2017**, *4*, 1639–1650. [CrossRef]
99. Richter, M.M. Electrochemiluminescence. In *Optical Biosensors*; Elsevier: Amsterdam, The Netherlands, 2008; pp. 317–384. Available online: https://www.elsevier.com/books/optical-biosensors/ligler/978-0-444-53125-4 (accessed on 26 March 2021).
100. Gao, J.; Chen, Z.; Mao, L.; Zhang, W.; Wen, W.; Zhang, X.; Wang, S. Electrochemiluminescent aptasensor based on resonance energy transfer system between CdTe quantum dots and cyanine dyes for the sensitive detection of ochratoxin A. *Talanta* **2019**, *199*, 178–183. [CrossRef]
101. Chen, H.; Li, W.; Zhao, P.; Nie, Z.; Yao, S. A CdTe/CdS quantum dots amplified graphene quantum dots anodic electro-chemiluminescence platform and the application for ascorbic acid detection in fruits. *Electrochim. Acta* **2015**, *178*, 407–413. [CrossRef]
102. Zhang, H.-R.; Xu, J.-J.; Chen, H.-Y. Electrochemiluminescence ratiometry: A new approach to DNA biosensing. *Anal. Chem.* **2013**, *85*, 5321–5325. [CrossRef]
103. Jiang, H.; Wang, X. Label free detection of folate receptor (+) cells by molecular recognition mediated electrochemiluminescence of CdTe nanoparticles. *Anal. Chem.* **2014**, *86*, 6872–6878. [CrossRef]
104. Liang, Z.; Zhang, Q.; Nie, Y.; Zhang, X.; Ma, Q. Polarized-Electrochemiluminescence biosensor based on surface plasmon coupling strategy and fluorine doped BN quantum dots. *Anal. Chem.* **2020**, *92*, 9223–9229. [CrossRef]
105. Wang, C.; Li, M.; Wang, P.; Liu, D. An electrochemiluminescence biosensor based on boron nitride quantum dots as novel coreactant for quantitative determination of concanavalin A. *Microchim. Acta* **2020**, *187*, 1–9. [CrossRef] [PubMed]
106. Hu, S.; Hidalgo, M.L.; Wang, F.C.; Mishchenko, A.; Schedin, F.; Nair, R.R.; Hill, E.W.; Boukhvalov, D.W.; Katsnelson, M.I.; Dryfe, R.A.W.; et al. Proton transport through one-atom-thick crystals. *Nat. Cell Biol.* **2014**, *516*, 227–230. [CrossRef] [PubMed]
107. Morishita, T.; Okamoto, H. Facile exfoliation and noncovalent superacid functionalization of boron nitride nanosheets and their use for highly thermally conductive and electrically insulating polymer nanocomposites. *ACS Appl. Mater. Interfaces* **2016**, *8*, 27064–27073. [CrossRef]
108. Chen, J.; Huang, X.; Sun, B.; Jiang, P. Highly thermally conductive yet electrically insulating polymer/boron nitride nanosheets nanocomposite films for improved thermal management capability. *ACS Nano* **2019**, *13*, 337–345. [CrossRef]
109. Wang, X.; Wu, P. Preparation of highly thermally conductive polymer composite at low filler content via a self assembly process between polystyrene microspheres and boron nitride nanosheets. *ACS Appl. Mater. Interfaces* **2016**, *9*, 19934–19944. [CrossRef] [PubMed]
110. Chen, J.; Wei, H.; Bao, H.; Jiang, P.; Huang, X. Millefeuille inspired thermally conductive polymer nanocomposites with overlapping BN nanosheets for thermal management applications. *ACS Appl. Mater. Interfaces* **2019**, *11*, 31402–31410. [CrossRef] [PubMed]
111. Lei, C.; Wu, K.; Wu, L.; Liu, W.; Du, R.; Chen, F.; Fu, Q. Phase change material with anisotropically high thermal conductivity and excellent shape stability due to its robust cellulose/BNNSs skeleton. *J. Mater. Chem. A* **2019**, *7*, 19364–19373. [CrossRef]
112. Han, J.; Du, G.; Gao, W.; Bai, H. An anisotropically high thermal conductive boron nitride/epoxy composite based on nacre-mimetic 3D network. *Adv. Funct. Mater.* **2019**, *29*, 1900412. [CrossRef]

113. Wang, T.; Wang, M.; Fu, L.; Duan, Z.; Chen, Y.; Hou, X.; Wu, Y.; Li, S.; Guo, L.; Kang, R.; et al. Enhanced thermal conductivity of polyimide composites with boron nitride nanosheets. *Sci. Rep.* **2018**, *8*, 1–8. [CrossRef]

114. Yuan, J.; Qian, X.; Meng, Z.; Yang, B.; Liu, Z.-Q. Highly thermally conducting polymer based films with magnetic field assisted vertically aligned hexagonal boron nitride for flexible electronic encapsulation. *ACS Appl. Mater. Interfaces* **2019**, *11*, 17915–17924. [CrossRef] [PubMed]

115. Zhou, S.; Xu, T.; Jiang, F.; Song, N.; Shi, L.; Ding, P. High thermal conductivity property of polyamide imide/boron nitride composite films by doping boron nitride quantum dots. *J. Mater. Chem. C* **2019**, *7*, 13896–13903. [CrossRef]

116. Beytur, M. Fabrication of platinum nanoparticle/boron nitride quantum dots/6-methyl-2-(3hydroxy-4-methoxybenzylidenamino)-benzothiazole (Ils) nanocomposite for electrocatalytic oxidation of methanol. *J. Chil. Chem. Soc.* **2020**, *65*, 4929–4933. [CrossRef]